Advanced Steel Construction – Vol. 22 No. 2 (2026) 181–197
DOI:10.18057/IJASC.2026.22.2.5

THEORETICAL FULL-PROCESS CALCULATION AND ANALYSIS FOR SUBCOMPONENTS IN END-PLATE-BOLTED BEAM-COLUMN JOINTS

Kang Ma [1,*], Yi-Ming Gao [1], Zhuo Wang [1], Ruo-Yang Wu [2], Hai-Feng Yu [1], Pan Xu [1] and Yong Li [1]

[1] *School of Civil Engineering, Hebei Province Housing Construction Projects Regeneration Technology Innovation Center, Hebei University of Science and Technology, Shijiazhuang 050018, China*
[2] *Consor Engineers, Herriman, Utah 84096, USA*
** (Corresponding author: E-mail: luya4426@126.com)*

ABSTRACT

Existing theoretical rotational curve calculation methods for end plate-bolted joints often overlook component-level load transfer mechanisms and full deformation processes. This paper introduces a full-process subcomponent analysis method, which systematically evaluates the force-deformation behavior of joint domains, bolts, end plates, and stiffeners at critical failure stages. Simplified models and formulas are developed to calculate the load-bearing capacity and rotation angles of each component. The proposed method was validated through experiments, numerical simulations, and a practical engineering case. The results show that the proposed method accurately predicts joint rotational behavior, with the end plate thickness and bolt configuration significantly influencing load distribution. By revealing the load transfer mechanisms and clarifying the physical meaning of each component's role in joint rotation, the findings of this study provide a robust theoretical foundation for holistic structural analysis and large-scale computation of steel structures.

ARTICLE HISTORY

Received: 5 December 2024
Revised: 7 July 2025
Accepted: 18 July 2025

KEYWORDS

End plate bolted joint;
Beam-column joint;
Full component process;
Theoretical calculation

1. Introduction

Steel structures have increasingly become the preferred choice for prefabricated construction due to their modularity and structural efficiency, with beam-column joints serving as crucial components for load transfer and overall stability. Among joint types, end-plate-bolt connections are widely adopted in steel construction because of their ability to resist both static and seismic loads through elastic-plastic deformation mechanisms [1]. These connections typically involve welding end plates to beam ends and securing them to column flanges with bolts, as illustrated in Fig. 1, which shows commonly used configurations such as double-extended, single-extended, and flush end plates [2,3].

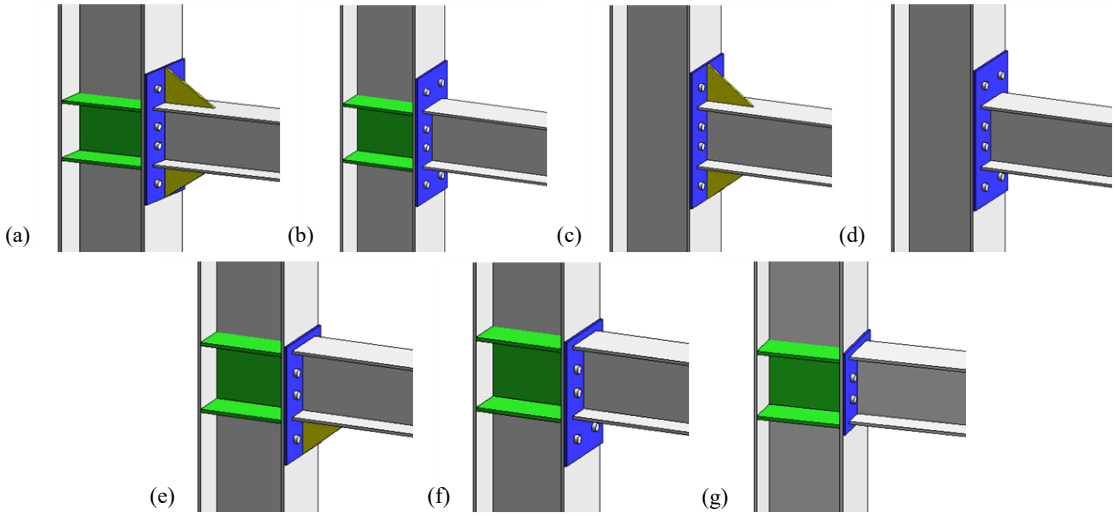

Fig. 1 Different types of end-plate-bolted joints. (a) Double-extended end plate with column web and end plate stiffeners;(b) Double-extended end plate with column web stiffeners; (c) Double-extended end plate with end plate stiffeners;(d) Double-extended end plate without column web or end plate stiffeners; (e) Single-extended end plate with column web and single-sided end plate stiffeners; (f) Single-extended end plate with column web stiffeners; (g) Flat end plate with column web stiffeners

Although previous studies on end-plate-bolted joints have significantly advanced our understanding of their overall mechanical behavior, two key limitations remain:

(i) Component-level mechanism gaps: Most studies have focused on global joint performance, overlooking the independent deformation characteristics and load-transfer mechanisms of subcomponents (e.g., joint domain, bolts, end plates, and stiffeners) across different loading stages (i.e., elastic, elastoplastic, and plastic).

(ii) Elastoplastic stage understudy: Although the elastic-stage capacity of individual components is well-documented, the subsequent elastoplastic deformation processes and their synergistic effects remain poorly understood [4-6].

To address these gaps, this paper introduces a full-process subcomponent analysis method that systematically evaluates the force-deformation behavior of four key components, namely, the joint domain, bolts, end plates, and stiffeners, from initial loading to ultimate failure. By integrating finite element analysis (FEA) with theoretical modeling, the proposed approach: develops simplified mechanical models for each component, delineating their deformation stages using stress-strain curve inflection points. Additionally, a component-wise superposition method is proposed to derive the joint's complete moment-rotation curve, accounting for both elastic and elastoplastic responses. The proposed model was validated through experimental tests and parametric studies on end plate/column flange thickness effects.

Unlike traditional component methods (e.g., EC3 [7,8]), which primarily focus on elastic-stage stiffness and ultimate capacity, this paper provides a unified framework for analyzing the full deformation process and component interactions. The findings of this study offer a robust theoretical foundation for optimizing joint designs in seismic-resistant steel structures, balancing computational efficiency with mechanical accuracy.

2. Calculation methods

2.1. Tests

2.1.1. Test specimen and loading configuration

In the tests, Q345 steel was used as the component material, with a column web stiffener thickness of 12 mm. The dimensions are shown in Figs. 2(a) and 2(b), which depict the beam-column joint configuration with a 10 mm thick 300 mm-wide end plate, M20 bolts, and an 83 mm bolt spacing. Low-cycle reverse loading was implemented using a self-balanced frame at the Structural Laboratory of Hebei University of Science and Technology, Hebei, China. As shown in Fig. 2(c), the test setup consists of a column horizontally fixed and a beam end loaded by a hydraulic actuator. The loading protocol followed the PRC industry standard Building Seismic Test Procedure JGJ/T101-2015 [8], as depicted in Fig. 2(c). In the figure, t_{ep} represents the end plate thickness, and t_{sr} represents the stiffening rib thickness.

2.1.2. Displacement point layout

The displacement measurement points were arranged as shown in Fig. 2(c). D1 was located at the center line of the loading, while D2 was positioned 250 mm away from the end plate. The difference in the measurement results between D2 and D1 was used to calculate the inclination angle of the steel beam. D3 and D4 were located at the lower flange of the column, while D5 and D6 were located at the upper flange of the column to measure the relative rotation of the joint domain. The calculation method followed the procedure outlined by Shi et al. [9].

2.1.3. Test phenomena and results

Observations of the loading process revealed that, at a displacement of 16 mm, yielding deformation occurred in the end plate accompanied by a noticeable separation from the column flange, as depicted in Figs. 3(a) and 3(b). As the displacement reached 64 mm, the end plate exhibited increased bending deformation, resulting in a more pronounced separation from the column flange, with a maximum bending deformation of approximately three times that observed at yielding. The displacement and load of the servo-hydraulic loading system were recorded, and the force-displacement hysteresis and skeleton curves were plotted, as shown in Fig. 3(c).

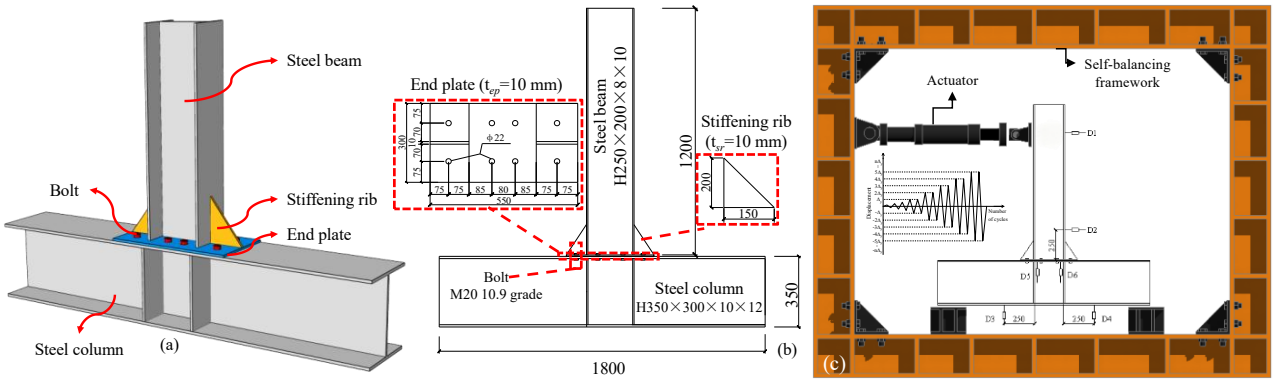

Fig. 2 Test joint diagram: (a) schematic; (b) dimension diagram; (c) test setup

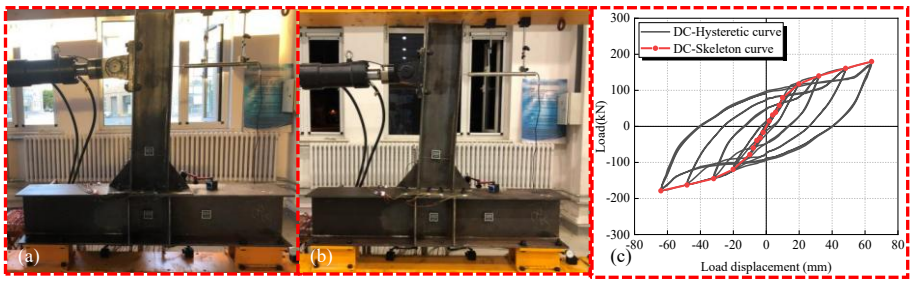

Fig. 3 Test phenomena for Δ = (a) 16 and (b) 64 mm.(c) Hysteresis and skeleton curves

2.2. Finite-element simulation

2.2.1. Modeling method

The material constitutive model adopts the von Mises yield criterion, which is defined as the equivalent stress that reaches the uniaxial tension yield stress when the material is subjected to a triaxial stress state, indicating the onset of yielding. Von Mises hardening was considered, with mixed hardening chosen as the hardening rule. The steel plate material properties are listed in Table. 1. Bonded constraints were selected for the welded connections, while surface contact constraints were chosen for components with only surface contact. Solid-model meshing was performed using C3D8R elements.

Table 1
Steel plate material properties

Steel plate thickness (mm)	Yield strength (N/mm^2)	Ultimate strength (N/mm^2)
12	373	504
10	356	488
8	329	456

When defining the contact properties of each contact component, binding constraints can be selected for welding, and surface-to-surface contact constraints can be selected for components with only surface-to-surface contact. When setting the binding or surface-to-surface contact constraints, it is necessary to define the contact pair and select the master and slave surfaces. The stable convergence calculation of the model is related to the master and slave surface selection.

The more symmetrical and regular the grid division, the better the model convergence and the faster the calculation progress. Additionally, this can effectively improve the numerical analysis accuracy. For parts with a simple stress distribution or less important parts, the mesh size can be increased, which reduces the calculation time. The bolt and hole division needs to be more regular, which facilitates convergence and improves the simulation accuracy.

In the test, bolts were utilized to fix the beam and column flanges, with three orthogonal translational displacement constraints ($U_x = U_y = U_z = 0$) applied to the bolt nodes to simulate rigid anchoring, as illustrated in Fig. 4(a). This figure shows the bolt constraints and loading configuration, where the bolt positions are fully fixed in all horizontal directions to mimic the experimental setup. For the loading mechanism, the entire beam end surface was kinematically coupled to a reference point, allowing the application of prescribed displacement loads at this point in strict accordance with the low-cycle reverse loading protocol specified in JGJ/T101-2015. This coupling strategy ensures uniform force distribution across the beam end, aligning with the test's loading characteristics and enabling accurate simulation of the cyclic deformation process.

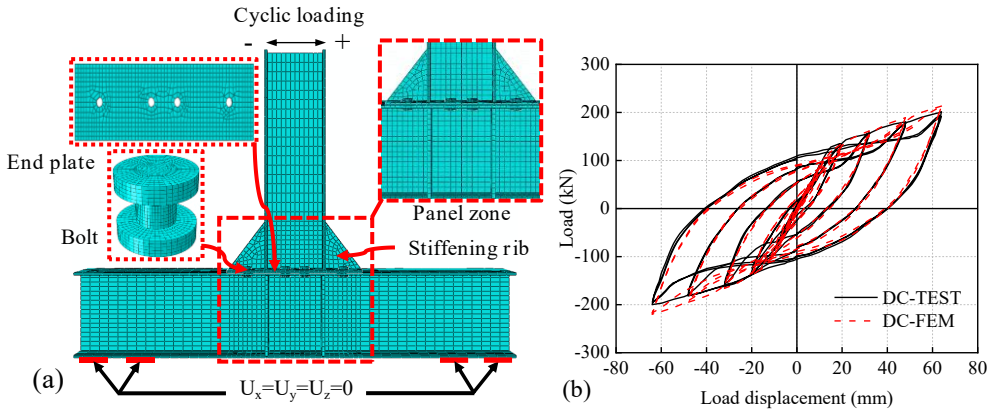

Fig. 4 Finite element simulation: (a) boundary conditions and loading positions; (b) test and simulation results

2.2.2. Finite element validation

A comparative analysis of the test (TEST) and finite-element model (FEM) simulation results of the hysteresis curves is presented in Fig. 4(b), which depicts the force displacement hysteresis loops and moment rotation curves of the specimens. As can be seen, the FEM results closely trace the TEST data, with both exhibiting nearly identical hysteretic shapes and key characteristic points (e.g., yield load, ultimate load, and post-peak deformation). Notably, the simulated end plate bending deformation and nut tilting phenomena shown in Fig. 4(b) align well with the experimental observations shown in Figs. 3(a) and 3(b), validating the FEM's ability to capture the joint's nonlinear behavior, including the stiffness degradation and energy dissipation characteristics under cyclic loading. This close agreement confirms the reliability of the numerical approach in predicting the mechanical response of end -plate-bolted joints. Both the TEST and FEM results exhibited phenomena such as end plate bending deformation, and nut tilt, as shown in Fig. 5, indicating that the established joint specimen model is reliable and accurate.

Based on the test and FEA results, 16 parametric FEMs were established to analyze the stress distribution and deformation properties of the joint domain, bolts, end plate, and reinforcement rib components during the loading process. Simplified stress analysis diagrams were generated to obtain a comprehensive theoretical moment-rotation calculation method. The established FEMs are listed in Table. 2.

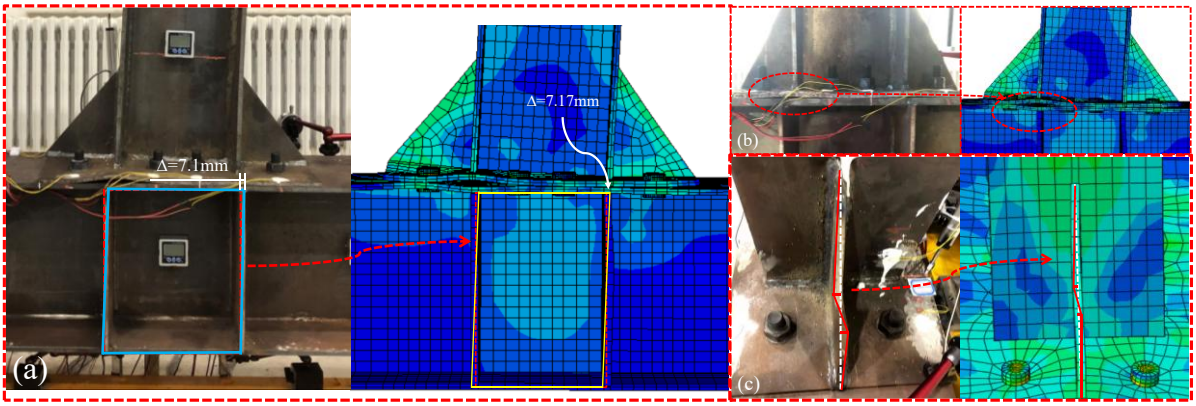

Fig. 5 Comparison between test and finite-element failure modes: (a) joint domain; (b) end plate; (c) stiffening rib

Table 2
Parametric finite-element models

No.	End plate thickness (t_{ep}/mm)	Column flange thickness (t_{cf}/mm)	Model components requiring analysis
1	12	12	Joint-domain, End-plate, Stiffener, and Bolt series
2	14	14	Joint-domain, End-plate, Stiffener, and Bolt series
3	16	16	Joint-domain, End-plate, Stiffener, and Bolt series
4	18	18	Joint-domain, End-plate, Stiffener, and Bolt series
5	20	20	Joint-domain, End-plate, Stiffener, and Bolt series
6	22	22	Joint-domain, End-plate, Stiffener, and Bolt series
7	24	24	Joint-domain, End-plate, and Bolt series
8		12	Bolt series
9	10	14	Bolt series
10		16	Bolt series
11		12	Bolt series
12	12	14	Bolt series
13		16	Bolt series
14		12	Bolt series
15	14	14	Bolt series
16		16	Bolt series

2.2.3. Mesh sensitivity analysis

To address mesh dependency, a comparative analysis of three mesh densities was conducted during finite-element modeling: (i) Coarse Mesh: Element size increased by 50% relative to the basis mesh; (ii) Basis Mesh: Reference mesh adopted in this study (C3D8R elements, regular division for bolts and holes); and (iii) Refined Mesh: Element size reduced by 50% relative to the basis mesh.

As shown in Fig. 6, the Basis Mesh demonstrates excellent agreement with the experimental results (TEST) [10], exhibiting initial rotational stiffness and ultimate moment deviations of less than 6% and 4%, respectively, which are within engineering tolerances. Using the Refined Mesh marginally improves accuracy (<2% deviation) but incurs a threefold increase in computational time. Furthermore, the Coarse Mesh significantly underestimates the ultimate moment (12% deviation) and exhibits stiffness divergence, confirming its inadequacy for reliable predictions. In conclusion, the Basis Mesh balances accuracy and computational efficiency, validating its use in the subsequent numerical analyses.

3. Results and discussion

3.1. Joint domain stress-deformation comprehensive analysis

3.1.1. Calculation sketch

The joint domain stiffness is a crucial parameter for assessing its deformation capacity. Pan et al. [11] suggested that when there is a significant disparity in the heights of the beam and column sections, the bending deformation of the joint domain should be considered in stiffness calculations. However, for standard beam and column dimensions, considering only shear deformation can yield sufficiently accurate results. For column joints with stiffeners, such as flange plates and web stiffeners, the stress deformation can be simplified to that of a short column under a moment couple, as illustrated in Fig. 7. The analysis was divided into the bending deformation of the column flange and shear deformation of the column web. The stress-deformation process of the joint domain was divided into three stages: elastic shear-bending deformation, yielding shear deformation, and post-yielding.

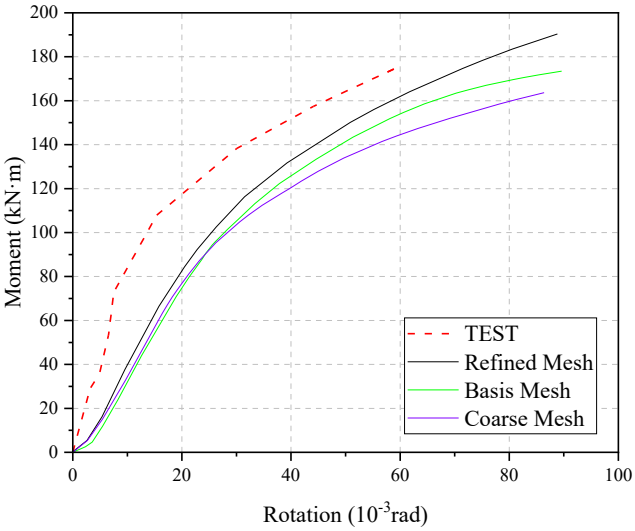

Fig. 6 Moment-rotation curves for the mesh sensitivity analysis

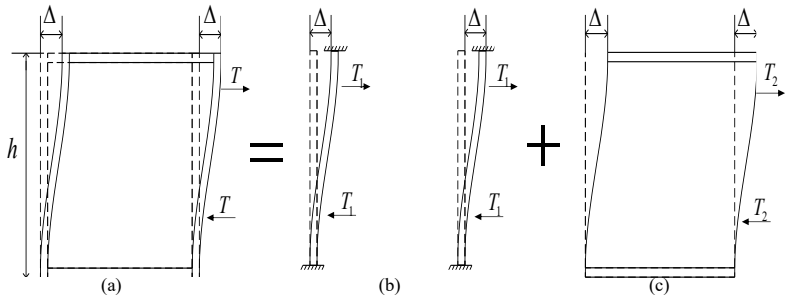

Fig. 7 Calculation diagram ($T = T_1+T_2$): (a) joint domain; (b) flange; (c) web plate

3.1.2. Elastic shear-bending deformation stage

The Chinese steel structure design code [12] provides a calculation method for the yield-bearing capacity of bidirectional bending joint domains. The following steps were taken to calculate the initial rotational stiffness of the joint domain in accordance with the bearing capacity calculation method provided by the steel structure design code.

First, the normalized width-to-thickness ratio of the prescribed joint domain $\lambda_{n,s}$ was determined as follows:

$$h_c/h_b \geq 1,\quad \lambda_{n,s} = \frac{h_b/t_w}{37\sqrt{5.34+4\left(h_b/h_c\right)^2}}\frac{1}{\sqrt{\frac{f_y}{235}}} \tag{1}$$

$$h_c/h_b \leq 1,\quad \lambda_{n,s} = \frac{h_b/t_w}{37\sqrt{4+5.34\left(h_b/h_c\right)^2}}\frac{1}{\sqrt{\frac{f_y}{235}}} \tag{2}$$

where h_b and h_c represent the beam and web calculation heights, respectively.

According to the normalized width-to-thickness ratio $\lambda_{n,s}$ of the joint domain subjected to shear, the shear strength f_{ps} of the joint domain was determined as follows:

$$\lambda_{n,s} \leq 0.6,\quad f_{ps} = \frac{4}{3}f_v \tag{3}$$

$$0.6 \leq \lambda_{n,s} \leq 0.8,\quad f_{ps} = \frac{1}{3}(7-5\lambda_{n,s})f_v \tag{4}$$

$$0.8 \leq \lambda_{n,s} \leq 1.2,\quad f_{ps} = \left[1-0.75(\lambda_{n,s}-0.8)\right]f_v \tag{5}$$

where f_v is the steel shear yield strength, $\lambda_{n,s}$ is the normalized width-to-thickness ratio of the joint domain subjected to shear, and f_{ps} is the joint domain shear strength.

The conversion relationship for the design strength values of the steel materials adopts the conversion relationships listed in Table. 3.

Table 3
Conversion relationships for the steel design strength

Material	Stress type		Conversion control
Steel	Tensile, compressive, and flexural resistance	Q235	$f = f_y/1.090$
		Above Q235	$f = f_y/1.125$
	Shear resistance		$f_v = f_y/\sqrt{3}$

The final bending capacity of the joint domain is as follows:

$$M_{b1}+M_{b2} \leq f_{ps}V_p, V_p = h_{b1}h_{c1}t_w \tag{6}$$

where h_{b1} and h_{c1} represent the height of the beam and column flange heights, respectively.

When the joint domain shear strain reaches the yield strain, $\gamma = \gamma_y$, the shear rotation angle of the joint domain reaches φ_{sy}. Therefore, the initial joint domain rotational stiffness for shear rotation is

$$K = K_i = \frac{M_{b1} + M_{b2}}{\varphi_{sy}} \tag{7}$$

To consider the shear deformation of the steel column webs and flanges under uniaxial bending conditions in the elastic stage, referring to Wang et al. [13-14], the joint domain rotational stiffness can be defined as follows:

$$K = \frac{T}{\Delta} l^2, \quad \tau = G\gamma, \quad \gamma = \frac{\Delta}{l} = \frac{f_y}{G}, \quad G = \frac{E}{2(1+\mu)} \tag{8}$$

$$T_1 = \frac{12EI_{cf}\Delta}{l^3} \tag{9}$$

$$T_2 = A_{cfb}\tau = \frac{A_{cfb}E\Delta}{2l(1+\mu)} \tag{10}$$

The initial joint domain rotational stiffness for shear rotation is:

$$K = K_i = \frac{l^2}{1+\frac{l}{H_C}}\left[\frac{12E(I_{cf1}+I_{cf2})}{l^3} + \frac{A_{cfb}E}{2l(1+\mu)}\right] \tag{11}$$

The corresponding bending capacity of the joint domain at this point is:

$$M = (2T_1 + T_2)l \tag{12}$$

where G is the steel shear modulus, E is the steel elastic modulus, E_h is the steel strain-hardening modulus, and H_c is the selected column segment length.

3.1.3. Yield shear deformation stage

After yield shear deformation in the joint domain, the joint domain rotational stiffness changed. For this type of change, referring to Krawinkler et al. [15], modifications were made to the corresponding calculation formulas for $\beta = 1\text{-}H_c/l$, as follows:

$$K = K_P = 1.3\times\left[\frac{12EI_{cf1}}{5t_{cf1}\beta} + \frac{12EI_{cf2}}{5t_{cf2}\beta}\right]\times\left(\frac{4\min\{t_{cf1}, t_{cf2}\}}{\max\{t_{cf1}, t_{cf2}\}}\right) \tag{13}$$

In this study, we assumed that the stiffness remains constant until the shear strain reaches $3\gamma_y$. Accordingly, the ultimate plastic moment at which this state is reached is:

$$M_p = K_i\gamma_y + 2K_p\gamma_y \tag{14}$$

where β is the adjustment coefficient for the shear's contribution to the joint domain shear resistance, l is the lever arm of the shear force in the joint domain, t_{cf} is the column flange thickness, and I_{cf} is the moment of inertia of the column flange section.

3.1.4. Post-yielding stage

For a joint domain exceeding the yield moment, as the material enters the strain-hardening stage, the coefficient is adjusted according to the stiffness in the plastic stage, as follows:

$$K = \frac{E_h}{E}K_i \tag{15}$$

where K is the joint domain rotational stiffness, E is Young's modulus, and E_h is the steel strain-hardening modulus.

3.1.5. Moment-rotation curve

The results obtained using the proposed theoretical calculation method were compared with the FEM and test results for validation. The comparison between the joint domain moment-rotation models is shown in Fig. 8. The FEM simulation and test results are in good agreement with the theoretical calculation results. However, as the column flange thickness increased, the relative error tended to increase, indicating that the simplified joint domain shear deformation model may underestimate the influence of geometric nonlinearity in thick-plate scenarios. This discrepancy is attributed to the theoretical model's neglect of three-dimensional (3D) stress states in the column flange and the actual welding residual stresses not being considered in the analysis.

The results obtained from the theoretical calculation method (TCM) described above were compared with the FEM and test results in a stage-by-stage basis to validate the proposed theoretical model. The comparison between the moment and rotation models is shown in Fig. 9.

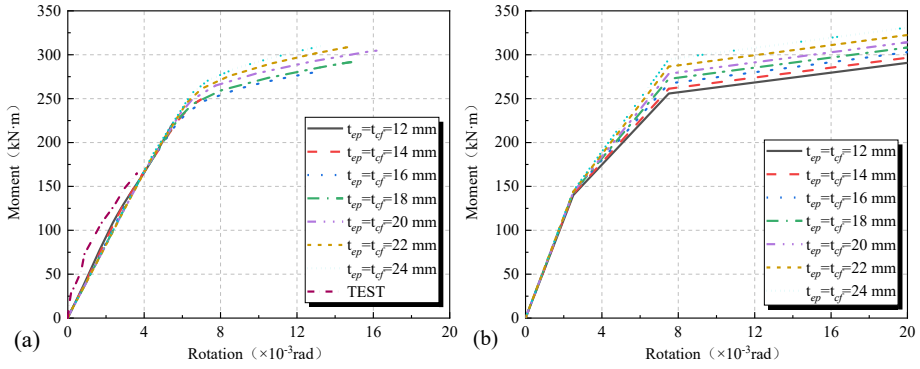

Fig. 8 Joint domain moment-rotation model: (a) finite-element simulation and test results; (b) theoretical calculation results

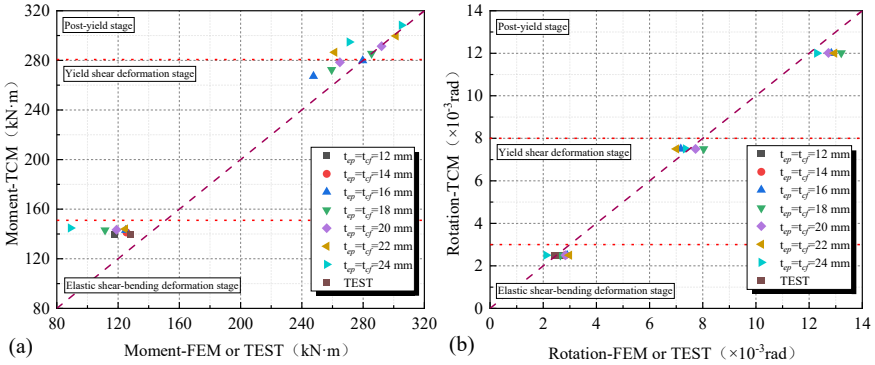

Fig. 9 Results for characteristic points of the joint domain. (a) moment; (b) rotation

3.1.6. Influence of material grade on the joint domain mechanical performance

Hysteretic Behavior

Under cyclic loading, the hysteretic curves of panel zones constructed with Q235, Q345, Q355, and Q460 steel were compared (Fig. 10). The results show that increasing the material strength leads to a marginal improvement in the energy-dissipation capacity, with the hysteretic loop area increasing by approximately 5%-8% from Q235 to Q460. However, this enhancement is significantly less than the theoretical strength increase, indicating that material strength is not the dominant factor governing the panel zone performance.

Mechanism Analysis

The limited improvement in the energy-dissipation capacity with increasing material grade is predominantly governed by local buckling, where panel zones exhibit out-of-plane deformation and instability (as visible in the test observations shown in Figs. 3 and 5) before fully utilizing the material's yield strength, particularly in thin-walled configurations ($t_{cf} \leq 16$ mm). This aligns with the theoretical model's acknowledged limitation in terms of underestimating the geometric nonlinearity and 3D stress states in thick plates, as discussed in Section 3.1.5, as buckling initiates at lower loads due to inherent geometric imperfections. Concurrently, welding residual stresses introduce initial tensile stresses near welds, accelerating plastic deformation and buckling onset, even in high-strength steels like Q460. Additionally, shear deformation dominance constrains the impact of material strength, as shear capacity scales less significantly with grade compared to tensile strength, and the panel zone's aspect ratio (h_b/h_c) limits shear-driven energy dissipation. Finally, stiffener configuration effects overshadow the material grade effects: increasing the stiffener thickness (t_{sr}) enhances the stability more effectively than upgrading the steel strength, as evidenced in the model's emphasis on geometric parameters for resisting buckling, whereas high-strength steel (e.g., Q460) alone cannot mitigate premature instability without corresponding thickness or stiffening adjustments.

Engineering Implications

For seismic design, prioritizing the stiffener configuration and thickness optimization is more effective than upgrading the material grade alone. While high-strength steel (e.g., Q460) may delay bolt failure, it does not mitigate panel zone buckling unless accompanied by increased plate thickness or stiffening. This aligns with the proposed full-process subcomponent method's emphasis on integrating geometric and material factors.

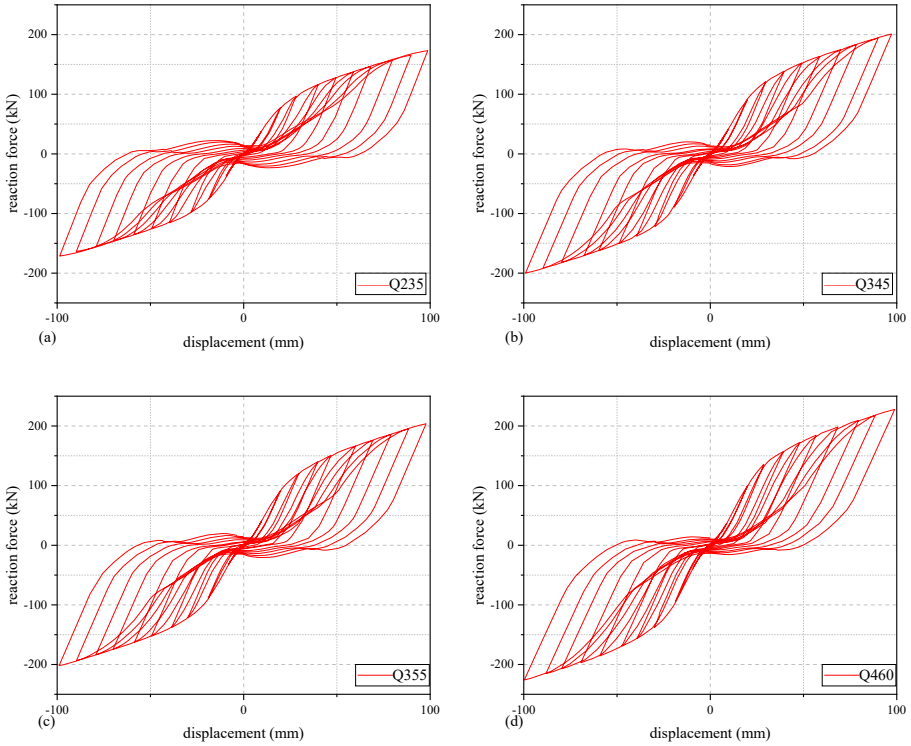

Fig. 10 Node hysteresis curves for steel with different strength grades: (a)Q235; (b)Q345; (c)Q355; (d)Q460

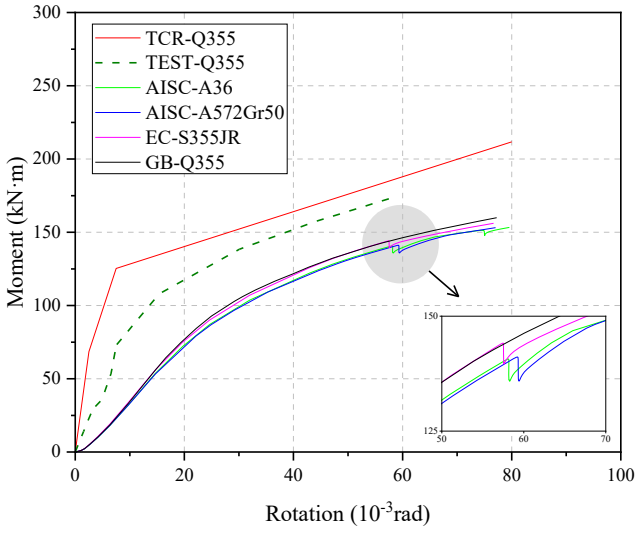

Fig. 11 Comparison of the bending moment and angle curves under different specifications

3.1.7. Validation extension to diverse steel grades

To address material validation limitations, the theoretical calculation method (TCR) was extended to steels from three design codes: Q355 (GB), A36/A572Gr50 (AISC), and S355JR (Eurocode) using ABAQUS simulations. The moment-rotation curves (Fig. 11) demonstrate close alignment between the TCR predictions, experimental data, and FEA results. Notably, the TCR consistently overestimates the experimental moments by 7%-10% at the same rotation angle, providing a conservative safety margin. This stems from its subcomponent superposition approach, which decomposes the joint into end plates, bolts, and panel zones. As shown in Fig. 11, the curves for different steel grades exhibit similar trends, verifying that the TCR can directly integrate material properties from any standard without empirical calibration. This modular design approach ensures generality for global engineering practice.

3.2. Comprehensive bolt stress and deformation analysis

When high-strength bolts with friction-type connections are used, pre-tensioning is necessary during tightening. This pre-tensioning induces compressive strain in the end plate and column flanges. As external loads are applied to the end plate, these compressive strains change. The stress state of the bolts in the tension zone could be categorized into three stages: contact, rigid separation, and complete separation between the end plate and column

flange.

3.2.1. End plate and column flange in the bolted zone in contact

After the bolts are tightened, a pre-tensioning force is generated, as shown in Fig. 12(a), which depicts the bolts in a state of initial tension that pulls the end plate and column flange tightly together. This creates a compressive force between the two plates, where the force from the bolt's pre-tension is balanced by the pressure between the plate surfaces.

When the end plate is subjected to external loads, it begins to separate from the column flange, as illustrated in Fig. 12(b). As the plates start to pull apart, the compressive force between them decreases, while the tension force in the bolt increases. As can be seen, the bolt is under higher tension due to the applied load, with the end plate slightly lifted from the column flange but still in partial contact. A comparison between Figs. 12(a) and 12(b) visually demonstrates how the bolt's tension increases as the joint transitions from a pre-tensioned state to one bearing external loads, highlighting the crucial role of bolt tension in resisting separation and maintaining joint integrity.

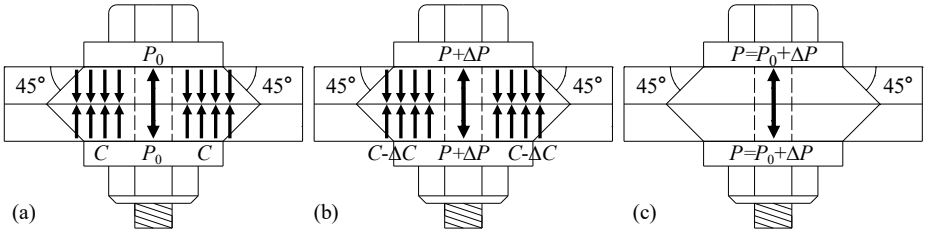

Fig. 12 Tensile force on the bolt's internal force: (a) only pre-tensioning force; (b) pre-tensioning force with tensile force; (c) pre-tensioning force disappeared

In the absence of external forces, the end plate and column flange are in contact. Under the action of a compressive force, the end plate and column flange undergo slight deformations. The pre-tensioning force of the bolt is in constant contact with the end plate and column flange. Therefore, the end plate, column flange, and bolt undergo slight deformations of the same magnitude. The slight deformation Δl caused by the compressive force can be calculated as follows:

$$P_0 = C, \quad \Delta l = \frac{C}{\lambda A_{bt'} E} L_{bt'} = \frac{P_0}{\lambda A_{bt'} E} L_{bt'} \tag{16}$$

When the end plate is subjected to a certain tensile force, separation occurs between the end plate and column flange. At this point, the decrease in the compressive force decreases the compressive microdeformation. However, the tensile force increases the tension force acting on the bolt. The change in tensile force F, actual increase in tension force ΔP, and bolt elongation Δl_i are calculated as follows:

$$F = \Delta P + \Delta C, \ \Delta P = \Delta l_i \cdot k_{bt}, \ \Delta l_i = \frac{\Delta C}{\lambda A_{bt'} E_{bt'}} \tag{17}$$

3.2.2. End plate and column flange in the bolted zone in the critical separation state

As shown in Fig. 12(c), at this point, the end plate is on the verge of separating from the column flange under the action of the tensile force, resulting in the absence of a compressive force between the end plate and column flange. The tension force T, elongation deformation Δl_i, and tensile strain ε_0 of the bolt are calculated as follows:

$$\Delta C = C = P_0, \ T = P_0 + \Delta P, \ \Delta P = \Delta l_i \cdot k_{bt}, \ \Delta l_i = \Delta l, \ \varepsilon_0 = \frac{\Delta l}{L_{bt'}} \tag{18}$$

where ε_0 is the bolt separation strain.

3.2.3. End plate and column flange in the bolted zone in a separation state

After reaching the state where the end plate and column flange are separated, the bolt stress and deformation calculation can be simplified and analyzed as the uniaxial tension of the bolt. Under the action of the tensile force, when the bolt reaches its tensile yield strength, the tension force T_i and resulting elongation deformation Δl_i of the bolt can be calculated as follows:

$$T_i = f_{bt',y} A_{bt'} \tag{19}$$

$$\Delta l_i = \frac{\Delta P}{E_{bt'} A_{bt'}} L_{bt'} \tag{20}$$

3.2.4. Bolt internal force and bending capacity calculation

After analyzing the stress and deformation of individual bolts under a tensile force, the effect of bending moment loads on individual bolts in the entire end-plate-bolt connection of the beam-column joint was further studied and analyzed. This involves establishing a relationship between the load on individual bolts and bending moment. This approach facilitates a better design of the load-bearing capacity of the bolts required in the end -plate-bolt connection joint.

First, based on the FEM results, the influence of the end plate and column flange thicknesses on the bolt internal forces was analyzed. Four bolt regions on one side were selected for analysis: the outer tension extension (BL), inner tension extension (NL), outer compression extension (BY), and inner compression extension (NY) regions. As shown in Fig. 13, as the end plate and column flange thicknesses change, there is a significant change in the bolt internal forces and maximum bending capacity of the joint. A comparison of the FEM simulation results revealed that the influence of the plate thickness variation on the development of the bolt internal forces was in stages, with 10-12, 12-16, 16-20, and 20-26 mm as the different stages. Therefore, stage points were selected for analysis.

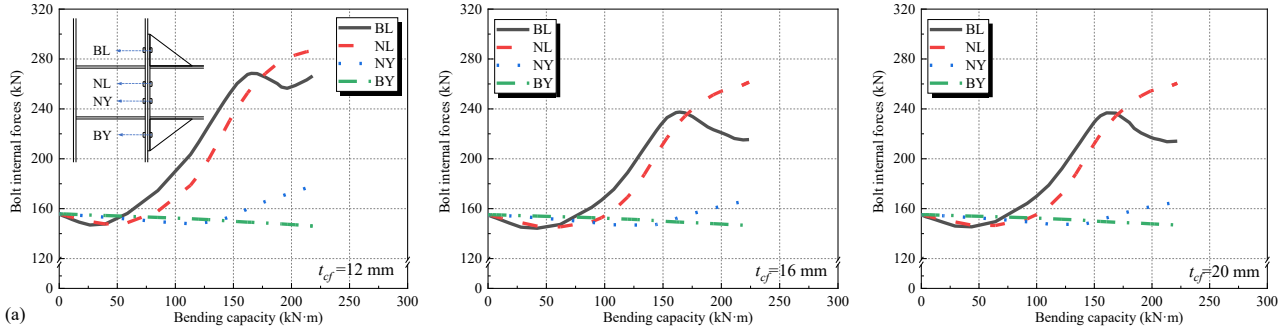

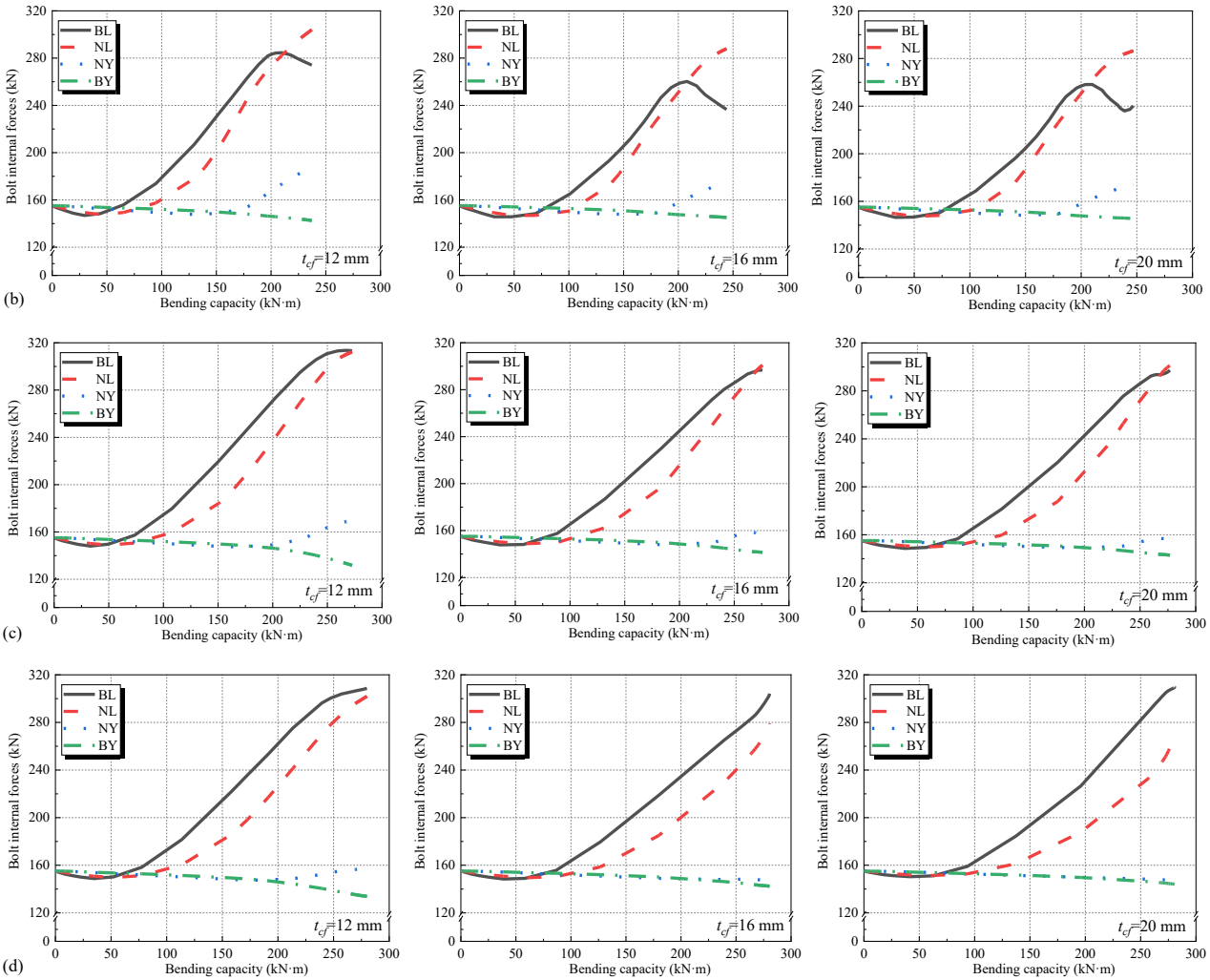

Fig. 13 Variations in bolt internal forces according to different end plate thicknesses (t_{ep}):(a)-(d) 10, 12, 16, and 20 mm, respectively

For an end plate thickness of 10 mm, the end plate fell within the thin plate range. As shown in Fig. 13(a), as the column flange thickness increases from 12 to 20 mm, the maximum internal force of the bolt on the inner side of the tension flange decreases gradually, similar to the maximum internal force of the bolt on the outer side of the tension flange. Initially, the bolt internal force on the outer side of the tension flange exceeded that on the inner side. However, after the bending moment reached 160 kN·m, the bolt internal force on the outer side of the tension flange began to decrease, indicating that the end plate underwent significant deformation at this point. The bolt internal force on the inner side of the compression flange continued to decrease when the bending moment was in the 0-150 kN·m range. However, when the bending moment reached 150 kN·m, the internal force began to increase, indicating that the bolt on the inner side of the compression flange was subjected to tension.

For an end plate thickness of 12 mm, the end plate still fell within the thin-plate range, and its stress and deformation were essentially the same as those for an end plate thickness of 10 mm. As shown in Fig. 13(b), as the column flange thickness increases from 12 to 20 mm, the variation in the bolt internal forces is similar to that at an end plate thickness of 10 mm. However, for an end plate thickness of 10 mm, the bolt internal force on the outer side of the tension flange was initially greater than that on the inner side. When the bending moment reached 160 kN·m, the internal force of the bolt on the outer side of the tensile flange decreased. For an end plate thickness of 12 mm, the bolt internal force on the outer side of the tension flange started to decrease only after the bending moment reached 200 kN·m.

For an end plate thickness of 16 mm, the end plate fell within the medium-thickness range, and its stress and deformation changed accordingly. As shown in Fig. 13(c), as the column flange thickness increases from 12 to 20 mm, the maximum internal forces of the bolts on both the inner and outer sides of the tension flange gradually decrease. Initially, the bolt internal force on the outer side of the tension flange exceeded that on the inner side. However, towards the end, the bolt internal force on the outer side of the tension flange became almost equal to that on the inner side. The bending moment required for the bolt on the inner side of the compression flange to experience tension increased as the column flange thickness increased.

For an end plate thickness of 20 mm, the end plate fell within the thick-plate range, and its stress and deformation changed further. As shown in Fig. 13(d), as the column flange thickness increases from 12 to 20 mm, the maximum internal force of the bolt on the inner side of the tension flange gradually decreases. However, the maximum internal force of the bolt on the outer side of the tension flange increased as the column flange thickness increased. The bolt internal force on the outer side of the tension flange was greater than that on the inner side, and the difference between them increased with the column flange thickness.

This analysis revealed that decreasing end plate and column flange thicknesses led to increased bolt internal forces under the same bending load, due to the lever effect in thin plates. Thicker end plates improved the bolts' load capacity, as they required a higher bending moment for plastic deformation. During joint rotation, bolts on the compressed inner side transitioned from no tension to tension, shifting the rotation center toward the compressed flange. The tensile forces in bolts on either side of the tension flange exhibited similar trends but differed by approximately 1.2 times. These trends varied with end plate thickness, requiring separate equations for thin, medium, and thick plates.

Previous studies and analyses have analyzed calculation models and formulas for force distribution on bolt groups[16]. Different design calculation methods are provided in the design codes of different countries for the bolt-group force distribution in the end-plate-bolted connections of beam-column joints. The parameters used in the equations are shown in Fig. 14.

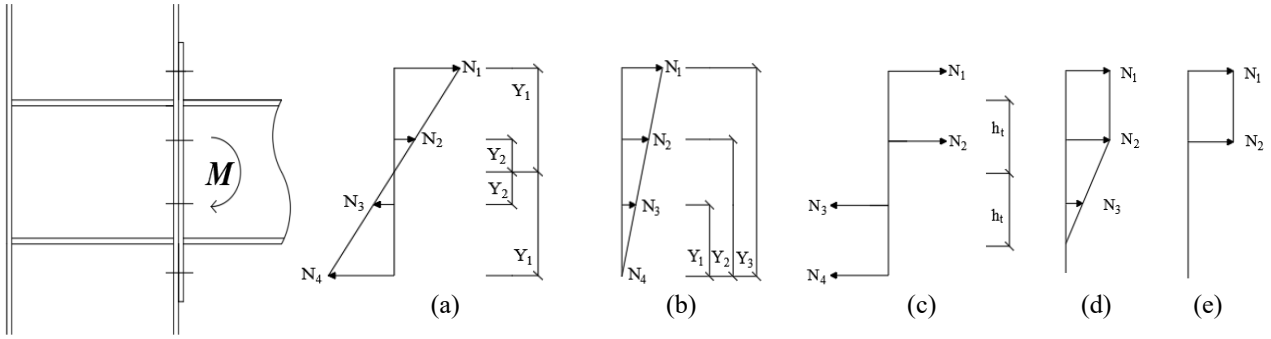

Fig. 14 Force distribution in bolt groups: (a) friction-type high-strength bolts [17]; (b) bearing-type high-strength bolts [17]; (c) JGJ 82-2011; (d) BS5950; (e) AISC358

In the Chinese Steel Structural Connection Joint Design Manual [17], the bolt-group force distribution in the end plate-bolted connections of beam-column joints under bending moment loads is divided according to bolt type: friction-type and bearing-type high-strength bolts. The maximum tensile force N_1 carried by a single row of bolts at different positions can be calculated as follows:

$$N_1 = \frac{My_1}{\sum y_i^2} \le N_t^b \tag{21}$$

In the Chinese Technical Specification for High-Strength Bolt Connections in Steel Structures (JGJ 82-2011) [18], the bolt-group categorization is not based on bolt type. Instead, it is divided based on the tension and compression zones. The maximum tensile force N_t carried by a single row of bolts in the tension zone can be calculated as follows:

$$N_t = \frac{M}{n_t h_t} \le N_t^b \tag{22}$$

In the British [20] and American [21] standards, the internal forces distribution in a row of bolts in a bolt group under bending moment loads can be calculated as follows:

$$M = \sum (N_t h) \tag{23}$$

where M is the bending-resistance capacity of the connection, n_t is the total number of bolt rows in the tension zone, N_t^b is the maximum tensile-load-bearing capacity of a single row of bolts, and h is the distance from each row of bolts to the pressure line of action.

By parametrically analyzing the relationship between the bolt internal forces and the joint bending-resistance capacity, as shown in Fig. 13, and considering existing specifications, the relationship between the bolt internal forces and the joint bending-resistance capacity can be redefined based on the end plate thickness. For thin plates, the method outlined in the Technical Specification for High-Strength Bolt Connections in Steel Structures was used, as shown in Fig. 15(a), with an additional factor of 1.2 to account for the influence of leverage forces. The calculation method for friction-type high-strength bolts outlined in the Connection Joint Design Manual was used for medium and thick plates.

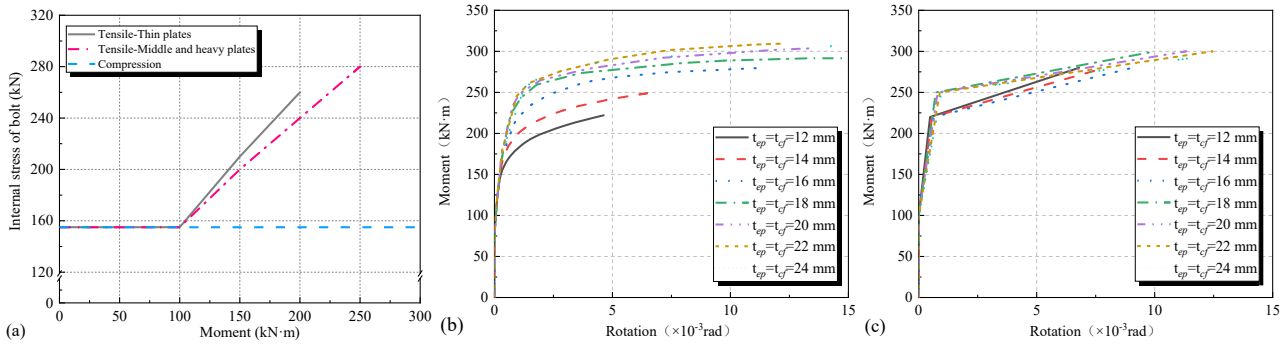

Fig. 15 Bolt moment-rotation curves. (a) bolt internal forces and joint bending resistance; (b) finite-element analysis results; (c) theoretical calculation results

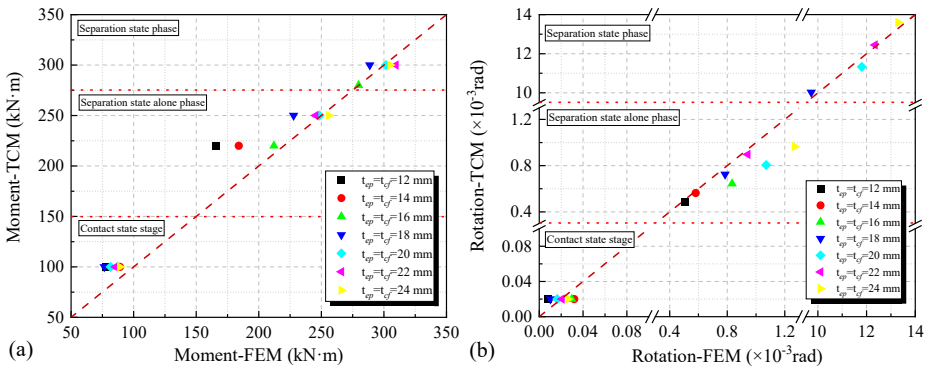

Fig. 16 Bolt results for (a) moment and (b) rotation.

3.2.5. Bolt moment-rotation curve

A comparison between the bolt moment-rotation models is illustrated in Figs. 15(b) and 15(c). As can be seen, the FEA results closely match the theoretical calculation results as the plate thickness increases [22]. However, as the end plate and column flange thicknesses decreased, the disparity between the results gradually increased [23]. This is primarily due to the

unaccounted "lever effect" caused by significant end plate bending, which amplifies bolt tension in reality but is overly simplified in the theoretical model. Conversely, for thick end plates (t_{ep}≥20 mm), the theoretical and numerical results closely align, suggesting that the model performs better when end plate stiffness dominates the deformation mechanism.

To validate the proposed theoretical model, the results obtained from the theoretical calculations (TCM) were compared with those from the FEM based on the aforementioned theoretical calculation methods. The results are shown in Fig. 16.

3.2.6. Parametric analysis for different bolt configurations

Three parametric bolt schemes (Plans A-C) and a control group were designed, with the configurations shown in Fig. 17 and parameters listed in Table 4. Fig. 18 shows their moment-rotation curves, demonstrating high similarity in ultimate capacity and stiffness degradation. As shown in Fig. 18, even with a 20% increase in outer-to-inner distance (Plan A) or a 25% reduction in inner spacing (Plan B), the curves remain nearly overlapping. This consistency arises from end plate geometric constraints (Fig. 17) and multi-component synergy, which dilute spacing effects.

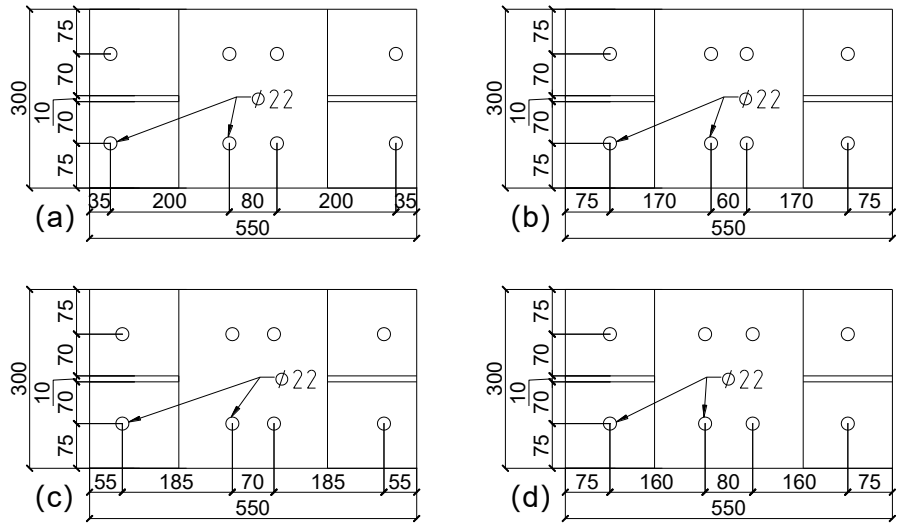

Fig. 17 End plate diagrams under different bolt arrangement plans: (a)-(c) Plans A-C, respectively; (d) TEST and Control group

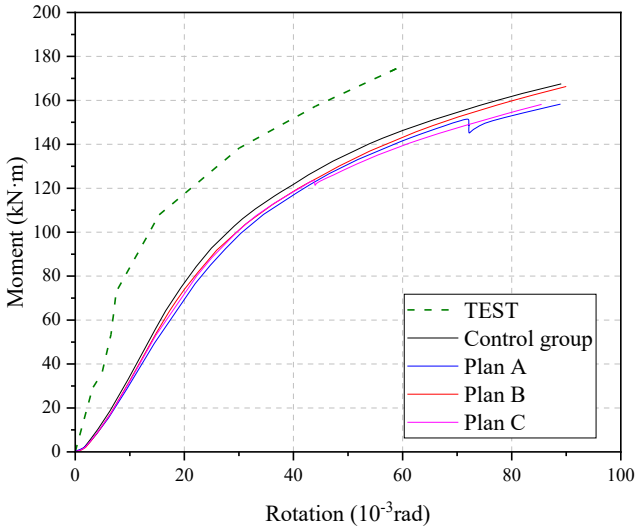

Fig. 18 Bending moment and angle curves under different bolt spacings

Table 4
Parameterization schemes for bolt spacing in the end plate node domain

Plan	Distance between the outer and inner center (mm)	Inner spacing (mm)	Inner moment arm (mm)
Control group	200	80	40
Plan A	240(+20%)	80(unchanged)	40(unchanged)
Plan B	200(unchanged)	60(-25%)	30(-25%)
Plan C	220(+10%)	70(-12.5%)	35(-12.5%)

TCR's modular framework accurately predicts responses for all configurations, as shown in Fig. 18, with deviations of ≤8% from the experimental data (TEST). The method's ability to accommodate local geometric adjustments is validated by the close match between the theoretical curves and FEA results, even for different bolt configurations (Fig. 18).

3.2.7. Failure mode analysis: bolt shear and flange buckling

Reasons for Neglecting the Bolt Shear Analysis

Parametric studies revealed that under pure bending or low-cycle reversed bending, the joint's load transfer is dominated by bending moments, inducing axial tension in bolts (via end-plate separation) rather than shear. Some key observations include the following:

(i) Moment-Driven Force Paths: Bolts in the tension zone resist tensile forces from end-plate rotation, while shear forces from beam shear are negligible.

(ii) Bolt Configuration: Symmetric bolt spacing (≤3d, where d is the bolt diameter) minimizes shear-induced slip, with stress distributions dominated by axial tension.

Flange Buckling in the Joint Domain

Stress distributions in the joint region confirm local buckling in column and beam flanges near the connection (Fig. 19), which arise from the following:

(i) Bending-shear coupling: The joint transfers combined bending and shear, inducing out-of-plane flexure in thin flanges (t_{cf}≤ 16 mm), consistent with stress concentration mechanisms discussed in Section 3.1.

(ii) Geometric discontinuity: The end plate connection creates stiffness transitions, concentrating stresses at the flange-end plate interface and triggering buckling, aligning with T-stub local buckling behavior in thin end plates.

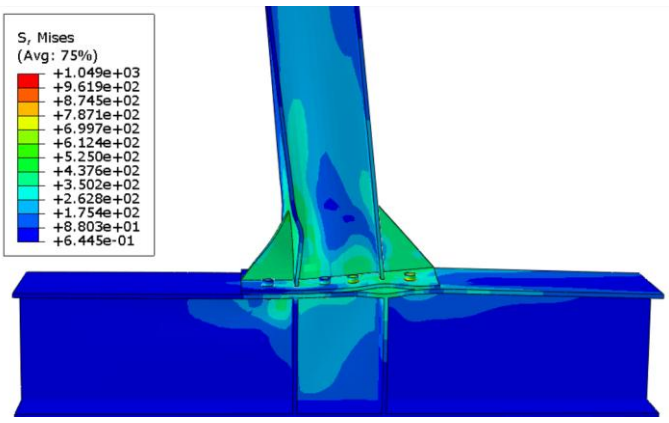

Fig. 19 Stress distribution revealing flange buckling in the joint region

3.3. Analysis of the entire bending process for end plates

To simplify the end plate-bolted connection failure analysis, previous researchers have proposed a method to simplify the end plate bending stress analysis by considering a T-shaped member composed of an end plate and a beam tension flange[24].

According to the Eurocode 3 standard [4], the failure of a T-shaped member can be divided into three types: plate yielding failure, bolt fracture failure, and plate-bolt combined failure. When the end plate thickness is small, plastic hinges may form at the end-plate-bolt and end-plate-beam tension flange connections, leading to end plate failure. This may result in plate yielding failure or plate-bolt combined failure, as shown in Figs. 20(a) and 20(c). When the end plate thickness is large, it may lead to bolt tensile failure, resulting in either bolt fracture or plate-bolt combined failure, as shown in Figs. 20(b) and 20(c). In this section, the analysis method for a T-shaped member is used to conduct theoretical research on the stress and deformation of the end plate and column flange under a bending moment load at the joint.

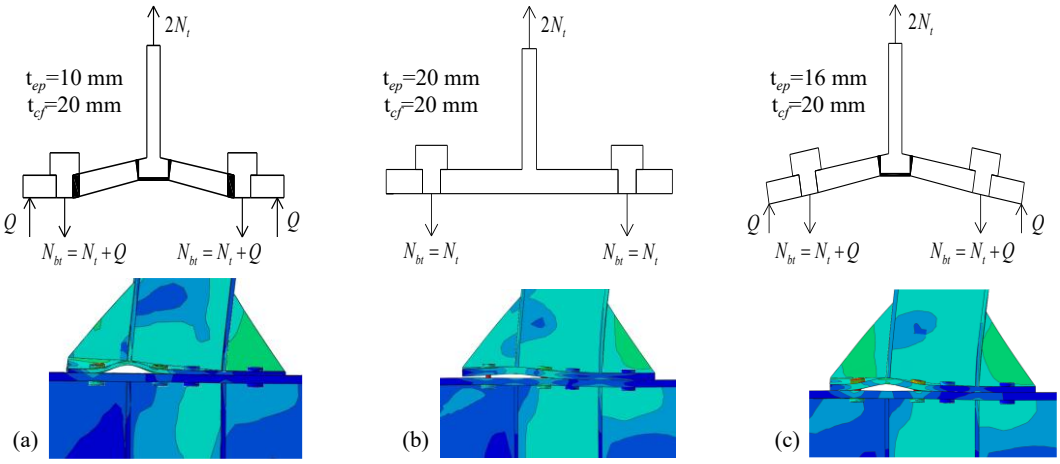

Fig. 20 Failure modes of the T-shaped component: (a) plate yielding; (b) bolt fracture; (c) plate-bolt simultaneous failure

To further illustrate the bending deformation and failure process of the end plate, we analyzed the plate buckling deformation through stagewise changes in the section load capacity. The specific analysis is as follows.

(1) Elastic stage

The mechanical model of the T-section used in this study is consistent with the EC3 simplification. However, for T-sections connected by high-strength bolts, the displacement due to the tensile force of the bolts was not considered. It was assumed that the restraint provided by the high-strength bolts acted as a fixed-end constraint. The theoretical calculation model of the T-section is shown in Fig. 21(a).

The theoretical initial flexural stiffness of the T-section is defined as the ratio of force N_t to the corresponding deformation in the elastic stage. According to structural mechanics principles, neglecting the shear deformation of the plates, the calculation of the corresponding deformation under the action of tensile force N_t can be determined using an equivalent simplified beam mechanical model, as follows:

$$\Delta=\frac{16N_t m^3}{192EI_T},\quad I_T=\frac{l_{eff}t_{ep}^{\ 3}}{12} \tag{24}$$

where I_T is the moment of inertia of the bent plate section of the T-section; I_{eff} can be calculated according to the provisions in EC3; and m is the distance from the center of the bolt hole to the intersection of the flange and web at the root.

The corresponding nodal rotation angle is calculated as follows:

$$\varphi=\frac{\Delta}{h_b} \tag{25}$$

where h_b is the beam height.

(2) Maximum elasticity in the elastic stage

The maximum elasticity-stage point is defined as the point at which the internal forces at the junction of the flange and end plates, as well as at the contact point of the bolt and end plate, reach the yield bending moment, as shown in Fig. 21(b). The yield bending moment at this point was calculated using the formulas defined in the EC3 specifications.

$$M_p=\frac{l_{eff}\times t_{ep}^{\ 2}\times f_y}{4} \tag{26}$$

where M_p is the plastic resistance moment of the equivalent T-section.

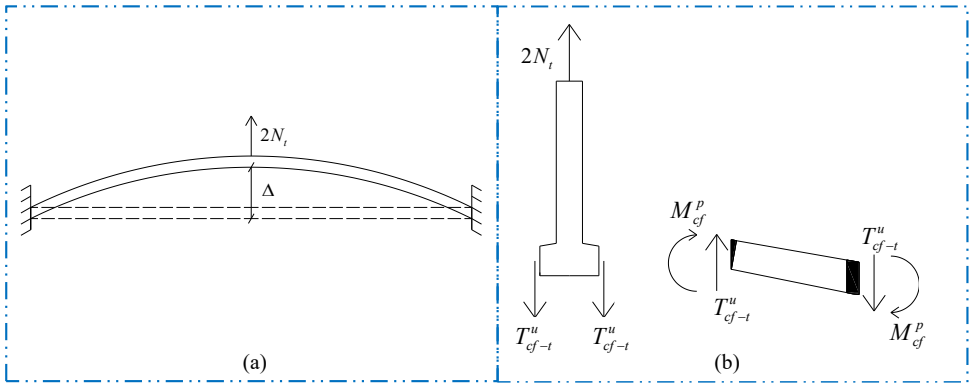

Fig. 21 T-section components: (a) Equivalent beam mechanical model; (b) Force diagram for yield deformation

The bearing capacity of the T-section flange segment under full flexural yield conditions was calculated as:

$$N_t=T_{cf-t}^u=\frac{M_p}{m} \tag{27}$$

Subsequently, the elastic stage of the end plate ends and enters the local plastic stage. For this stage, the stiffness change is defined as $10/t_{ep}$ multiplied by the initial stiffness, considering the influence of the end-plate thickness on the stiffness change in the local plastic stage.

(3) Point at which the entire cross-section of the end plate yields

The calculation of the end plate's bearing capacity according to the Chinese Technical Specification for Light Steel Structures of Portal Frame Buildings (GB 51022-2015)[25] was divided into the following four categories, with specific parameters as defined in the specification:

Category I: Extended Arm: $$N_{ut} = \frac{b_{ep} t_{ep}^2 f_y}{4e_f} \tag{28}$$

Category II: Ribless: $$N_{ut} = \frac{(0.5a + e_w) t_{ep}^2 f_y}{2e_w} \tag{29}$$

Category III: Both Sides Supported: $$N_{ut} = \frac{b_{ep} t_{ep}^2 f_y}{4e_f} + \frac{(e_f + e_w) t_{ep}^2 f_y}{2e_w} \tag{30}$$

Category IV: End-plate Section with Three-Sided Support:

$$N_{ut} = \frac{b_{ep} + 2b_s t_{ep}^2 f_y}{4e_f} + \frac{e_f t_{ep}^2 f_y}{e_w} \tag{31}$$

According to relevant literature, the stiffness changes to one-seventh of its original value until the plastic limit bending capacity is reached. In this study, for thin, medium, and thick plates, the plastic limit bending capacities were taken as 1.5, 1.5, and 1.1 times the plastic bending capacity, respectively. The change in stiffness after the yielding stage was calculated based on the stiffness variation in the joint domain.

(4) End plate moment-rotation curve

A comparison of the end plate moment-rotation models is depicted in Fig. 22. As can be seen, for thinner plates, there is a close agreement between the FEM results and the theoretical calculations. However, as the plate thickness increased, the discrepancies gradually increased. This may be because the simplification of T-shaped components ignores the spatial interaction between the end plate and the column flange, as well as the strain-hardening behavior of the steel in the post-yield stage. These factors result in insufficient representation of the actual load-bearing capacity of the end plate under complex stress states, highlighting the need for precise 3D modeling in future research.

Based on the aforementioned theoretical calculation methods, the results obtained from these methods (TCM) were compared with those from finite the FEA and tests (TEST) at different stages to validate the proposed theoretical model. The results of the moment and rotation models are presented in Fig. 23.

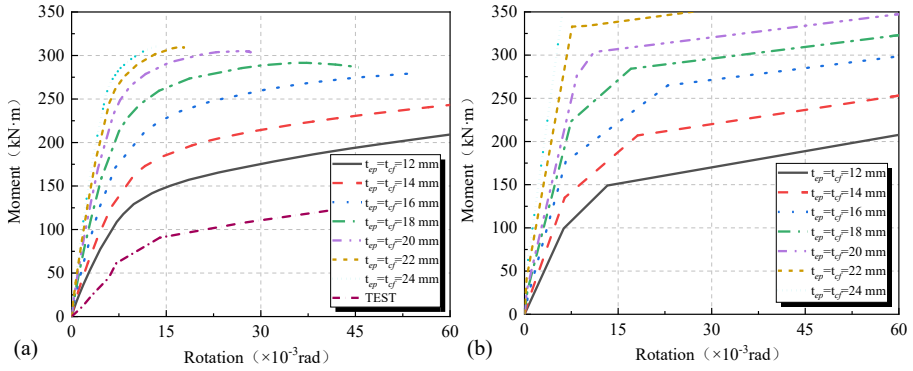

Fig. 22 Comparison of the end plate moment-rotation models: (a) finite-element and test results; (b) theoretical calculations

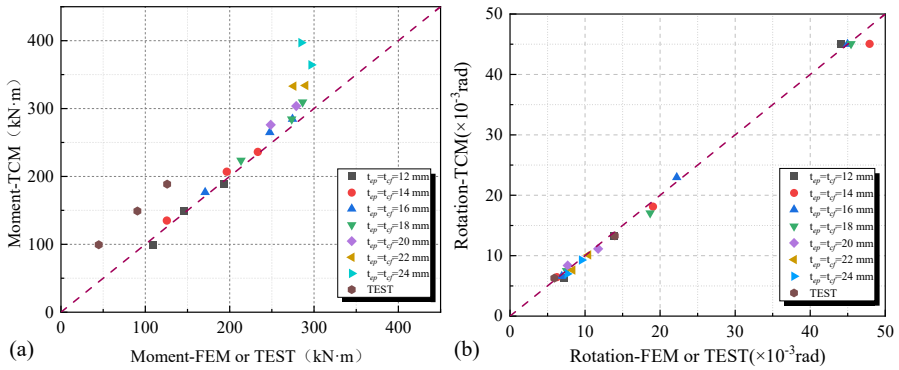

Fig. 23 End plate results for (a) moment and (b) rotation

3.4. Extended validation on end plate geometries

(1) Applicability to extended end-plate configurations

To validate the theoretical calculation method (TCR) across different end-plate geometries, ABAQUS simulations were conducted for four configurations: double-extended (DE), single-extended with tension on the extension side (SE-T), single-extended with compression on the extension side (SE-C), and flush (FLAT). Fig. 24 illustrates the geometric definitions of the DE, SE, and FLAT end-plate configurations, while Fig. 25 compares their moment-rotation curves. The simulation results reveal high consistency in the moment-rotation trends of the DE, SE-T, and SE-C configurations, indicating that TCR's subcomponent modeling framework, which focuses on the overall mechanical transmission of end plates, bolts, and panel zones, applies to extended end plate joints.

Notably, although SE-T and SE-C exhibit different force states on the extended side, the deformation coordination between the end plate and bolt system weakens the influence of single-side force differences, as evidenced by the overlapping curves in Fig. 25. This consistency confirms that TCR's modular approach, which decomposes the joint into independent subcomponents (end plate, bolts, panel zone), accurately captures the global mechanical behavior of extended configurations regardless of local force asymmetries. The subcomponent superposition principle allows TCR to maintain predictive accuracy by summing contributions from each element, as validated by the close alignment between the simulated and theoretical curves.

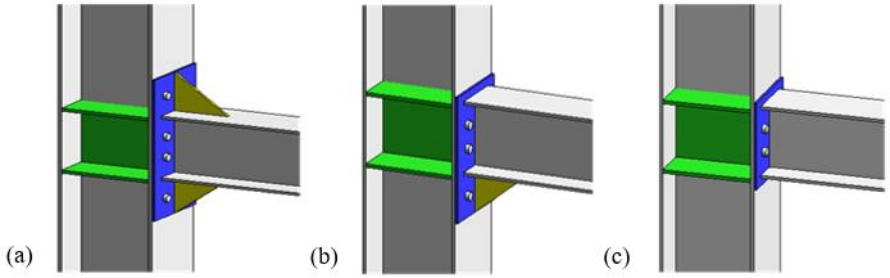

Fig. 24 Different end-plate geometries: (a) DE; (b) SE; (c) FLAT

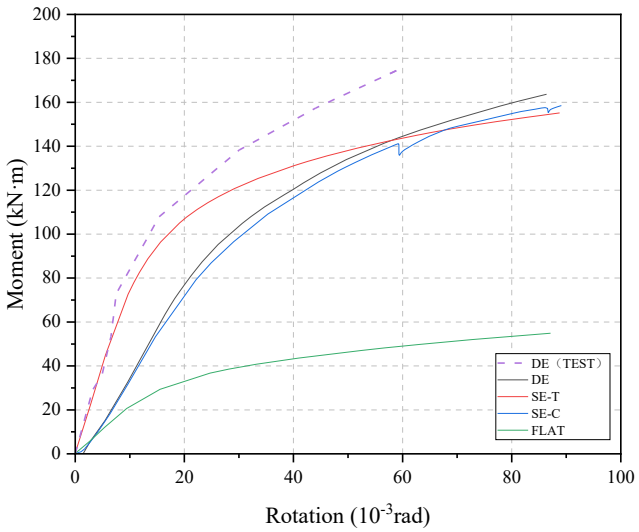

Fig. 25 Comparison between the bending moment and angle curves under different end-plate geometries

(2) Flush end plate load capacity decline mechanism

The FLAT end-plate configuration in Fig. 24 exhibits a significant decline in load-bearing capacity compared to the extended types, as shown by the abrupt stiffness degradation in Fig. 25. Unlike the DE and SE configurations, which use the extended segment to form a lever arm for dispersing bolt tension, the FLAT end plate relies on local bending near the bolts to resist moments. This leads to concentrated stress on the bolts and early local end-plate instability.

An analysis of the moment-rotation curves reveals that the FLAT end plate's rapid capacity decline stems from the absence of the lever effect present in the extended configurations. For approximate calculations using TCR, the effective bending length of the FLAT end plate is shorter, and local deformation is more pronounced. Therefore, the flexural stiffness of the end plate subcomponent can be adjusted by referencing the DE model: reducing the effective width coefficient to reflect the mechanical characteristics of FLAT configurations. This adjustment aligns the theoretical curve with the simulated response, leveraging TCR's modular framework to accommodate geometric variations by modifying subcomponent parameters without altering the overall modeling approach.

3.5. Stiffening rib-compression process analysis

After analyzing the stress variations in the rib-compression process based on multiple FEMs, the primary stress variations in the compressed region of the rib could be categorized into three stages: (i) initial yielding of one-third; (ii) two-thirds yielding in the second stage; and (iii) overall yielding in the third stage, as shown in Fig. 26.

As the applied bending moment increased and the joint gradually began to rotate, the rotation center of the beam end shifted. As shown in Fig. 27, the compressed region of the beam web (depicted in black) gradually moves from the middle position of the beam web towards the compressed flange of the beam (shown as the upper flange in Fig. 27) as the displacement load increases. Eventually, the compressed load was entirely borne by the compressed flange and ribs, with the black portion concentrated at the compressed flange. Therefore, the rotation center was defined as the compressed beam flange. In this section the stress distribution changes of the compressed ribs are analyzed. The compressed load distribution was determined based on the welded area ratio between the compressed beam flange and rib end plate.

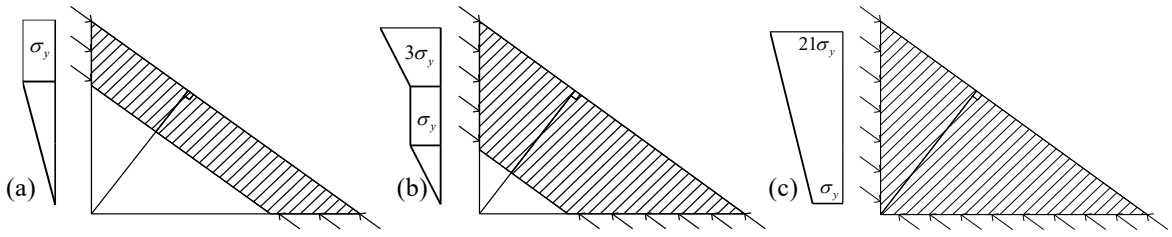

Fig. 26 (a) 1/3 stiffening rib compression yield; (b) 2/3 compression yield; (c) overall compression yield

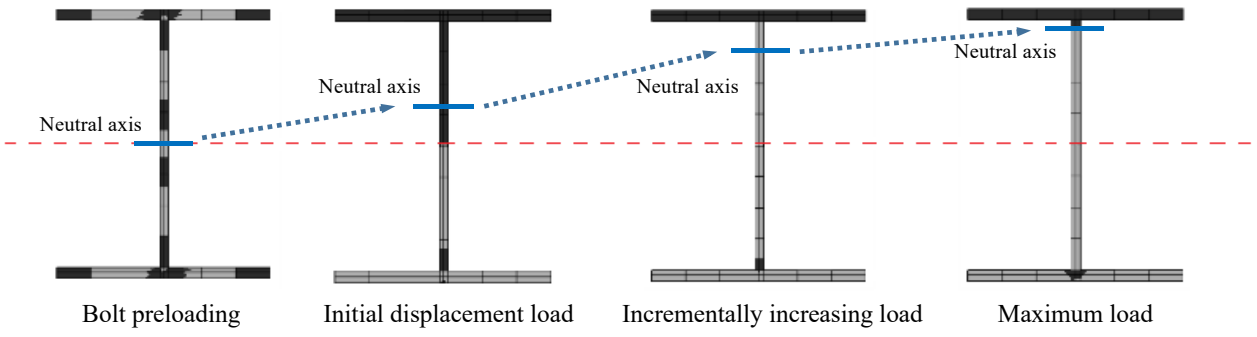

Fig. 27 Joint compression-zone variation diagrams

By combining the yielding states and stress development, the stress distribution along the diagonal of the stiffener can be calculated for the first two stages as follows:

$$P_{\mathrm{sy1x}} = \frac{1}{3} f_{\mathrm{psr,y}} h_{trangle} t_{\mathrm{psr}} \tag{32}$$

$$P_{\mathrm{sy2x}} = \frac{7}{6} f_{\mathrm{psr,y}} h_{trangle} t_{\mathrm{psr}} \tag{33}$$

where $h_{trangle}$ is the perpendicular distance from the intersection point on the right side to the diagonal.

In the third stage, the ultimate bearing capacity was calculated based on the cross-section of the triangular stiffener. Under bending moment loading, the contribution of the stiffener stress deformation to the rotation angle of the end-plate bolted connection of the beam-column joint can be calculated as follows:

$$\phi = \arctan\left(\frac{\varepsilon l_d}{l_{psr,s}}\right) \tag{34}$$

where ε is the oblique edge strain and l_d represents the length of the triangular stiffener diagonal. For the first, second, and third stages, ε was at maximum elastic strains of 1.5, 3, and calculated based on the calculated bearing capacity, respectively.

The stiffener bending moment-rotation model results are shown in Fig. 28, where the theoretical calculations based on the proposed method are compared with the FEM analysis results. As can be seen, for thinner plates, the FEM analysis results closely match the theoretical calculations; however, as the plate thickness increases, the discrepancies gradually become more significant.

Based on the theoretical calculation methods described above, the results (TCM) were compared with the FEM and test (TEST) results at different stages to validate the proposed theoretical model. The comparison results for the bending moment and rotation angle models are shown in Fig. 29.

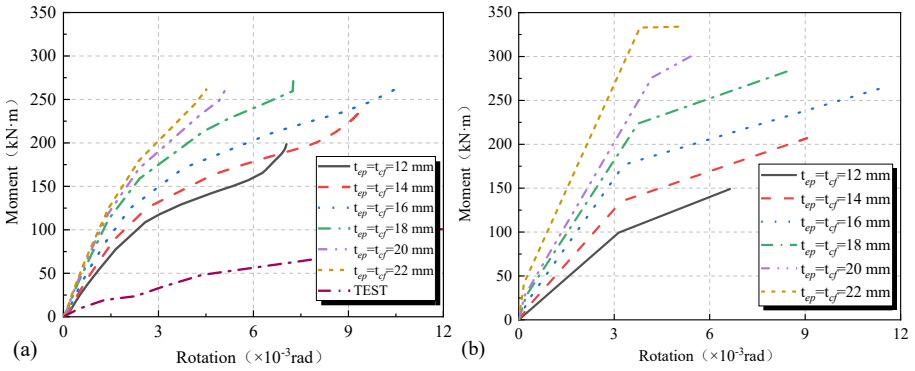

Fig. 28 Comparison between the stiffening rib moment-rotation models: (a) finite-element and test results; (b) theoretical calculations

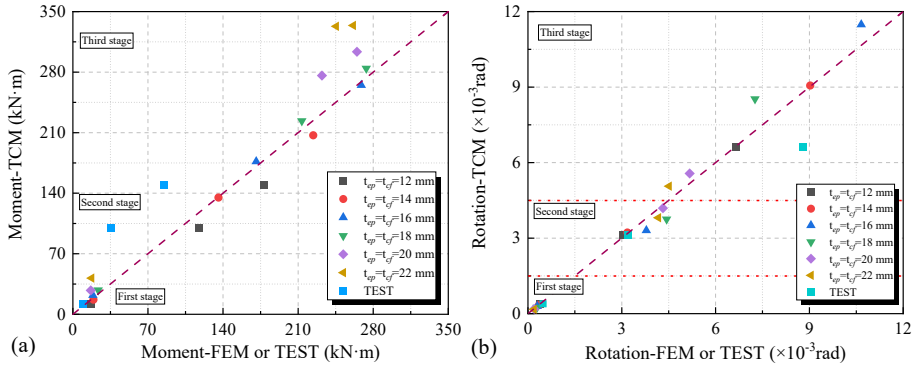

Fig. 29 Stiffening rib results for (a) moment and (b) rotation

3.6. Dynamic cyclic loading analysis: seismic applicability validation

To evaluate the proposed method's suitability for seismic design, dynamic (acceleration-driven) and quasi-static (displacement-controlled) cyclic loading simulations were conducted in ABAQUS. The simulations aimed to assess the joint behavior under inertial effects while maintaining consistent displacement amplitudes between loading types.

(1) Simulation setup

The quasi-static loading followed the JGJ/T101-2015 low-cycle reversed displacement protocol and serves as the baseline for static-mechanism validation. Meanwhile, for the dynamic loading, periodic acceleration histories were applied to induce inertial forces, mimicking seismic loading characteristics without direct seismic wave input. The loading frequency and amplitude were tuned to replicate earthquake-induced dynamic responses.

(2) Hysteresis curve comparison

In the quasi-static response, the hysteresis loops exhibited symmetric energy dissipation with stable stiffness degradation (Fig. 30(b)), aligning with the method's component-level superposition assumptions. In the dynamic response, the hysteresis loops exhibited pronounced pinching and scattering (Fig. 30(a)) due to inertial effects, but key mechanical features (e.g., yield displacement and post-peak deformation) remained consistent with the quasi-static trends. This confirms that core force-transfer mechanisms (e.g., bolt tension and end plate bending) are invariant under dynamic loading.

(3) Stress distribution and mechanistic robustness

Dynamic loading intensified the local stress gradients near bolt holes; however, primary stress concentrations at bolt interfaces and end plate-column junctions matched the static-mechanism predictions. The proposed method's applicability to seismic design is rooted in the following:

(i) Component-Level Invariance: Subcomponent superposition captures fundamental deformation mechanisms dominant in both static and dynamic scenarios.

(ii) Inertial Effect Integration: Treating dynamic inertial forces as equivalent static loads via D'Alembert's principle enables static-equivalent analyses, maintaining consistency with the FEA for key performance indicators (e.g., rotational stiffness trends).

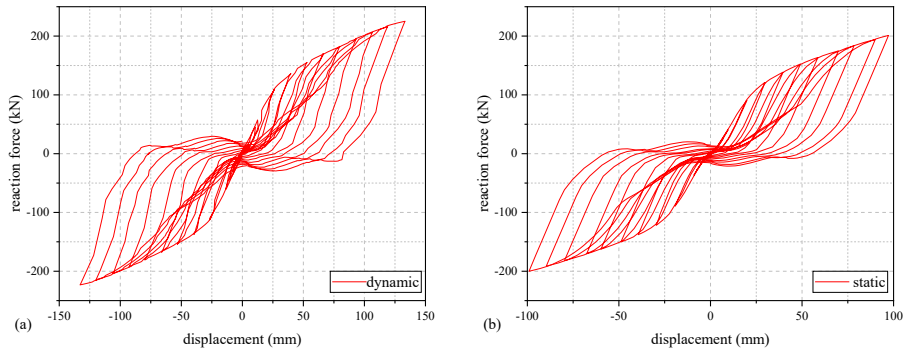

Fig. 30 Hysteresis curves: (a) Dynamic hysteresis curve (acceleration-driven); (b) Quasi-static (displacement - controlled)

3.7. Comparison with existing methods

Özkılıç et al. [5,6] focused on T-stub and end plate connection capacities but overlooked component-level deformation stages. Their models underpredict bolt tension in thin plates (40%-60% error) and oversimplify thick-plate stress states. To overcome these drawbacks, a full-process subcomponent approach is introduced in this paper, decomposing joint rotation into panel-zone, bolt, and end plate contributions. Additionally, Wang et al. [1] analyzed CFST column joints, but their study lacked generality for pure steel frames. In this study, the approach is generalized to steel joints, separating rotation into component contributions (panel zone: 30%-40%; bolts: 20%-30%), whereas Wang et al. [1] focused on concrete-confinement effects.

In conclusion, one of the main contributions of the proposed method lies in capturing component interactions and full deformation processes, unlike previous studies [1,5,6] that focused on isolated behaviors. This enables a systematic design; nevertheless, refinements for thick plates and CFST applications are still required.

4. Full bending moment-rotation angle curve validation

4.1. Validation of full-process bending moment-rotation curves of subcomponents via finite-element simulations

The theoretical calculation results of each component were synthesized to obtain the full-process subcomponent calculation results (TCM). These were then compared with the FEM results to validate the proposed theoretical model. The comparison results of the bending moment-rotation angle model are shown in Fig. 31.

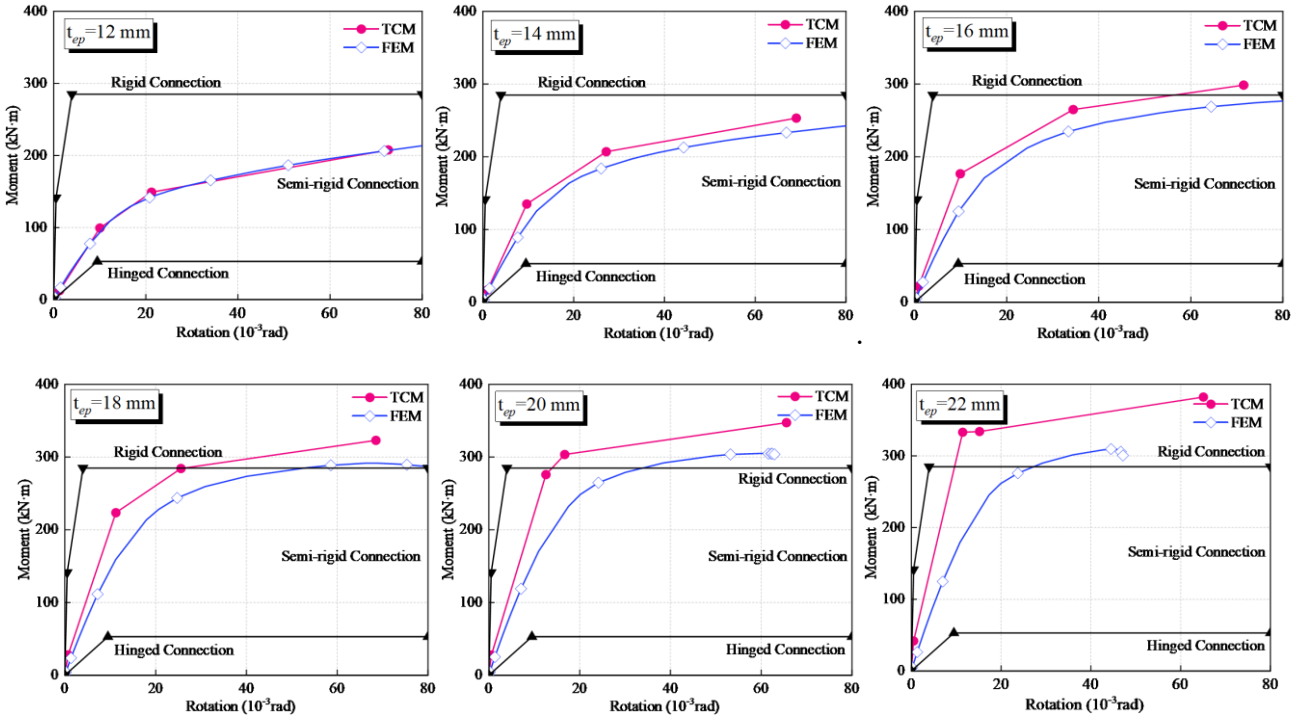

Fig. 31 Joint moment-rotation curve results

As can be observed in Fig. 31, the proposed method is more suitable for end plate connections of thin to medium thickness. However, for end plates with thicknesses greater than 20 mm, significant errors were observed in the calculations. This is attributed to the independent modeling of components without fully considering their synergistic effects—for example, the interaction between bolt tension and joint domain shear deformation. Experimental comparisons (Fig. 32) further indicate that the model's accuracy decreases with increasing loading complexity, highlighting the need for refined modeling of the contact nonlinearity and material ductility in future studies.

4.2. Validation of existing tests on end-plate-bolted beam-column joints

A comparison between the test results obtained by Sun et al. [25,26] and Zheng et al. [27,28] and those obtained with the proposed method is presented in Fig. 32. As can be seen, the theoretical values closely match the test data, indicating high accuracy and precision in terms of predicting the results of existing tests. This suggests that the proposed calculation method can accurately predict the full moment-rotation curve of the end-plate-bolted connection beam-column joints.

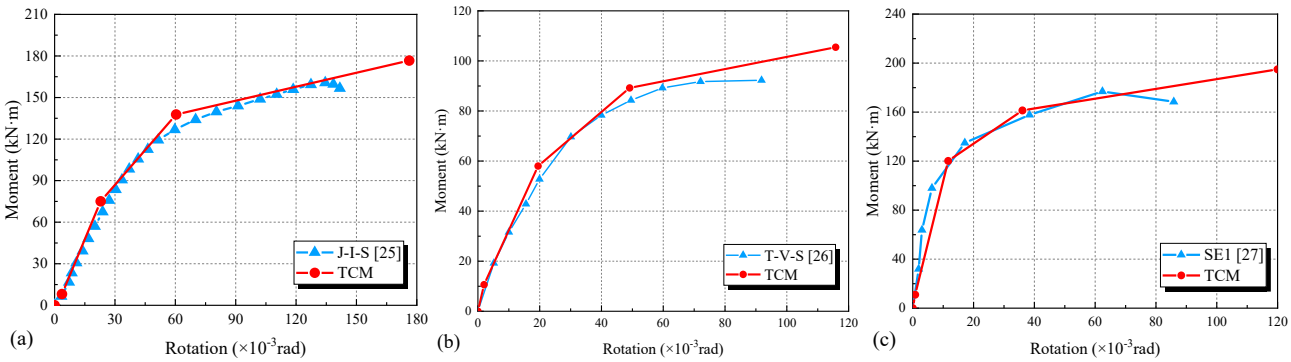

Fig. 32 Comparison between the proposed method and the other tests results from the literature: (a) J-I-S [25] ; (b) T-V-S [26] ;and (c) SE1 [27]

5. Engineering application and design guidelines

5.1. Design flowchart for subcomponent analysis

A systematic design flowchart (Fig. 33) is proposed to translate theoretical insights into practical engineering steps, outlining a modular approach to joint design. The proposed design flowchart involves the following:

(i) Decomposition: Joints are broken down into five subcomponents —joint domain, end plate, bolt group, column flange, and stiffeners.

(ii) Stage-wise analysis: Each component is evaluated through critical deformation stages (e.g., bolt tension from contact to full separation).

(iii) Superposition: Component rotations are synthesized to derive the joint's moment-rotation curve.

(iv) Validation: The results are cross-checked against design codes (e.g., EC3 and AISC) for compliance.

5.2. Key design guidelines for subcomponents

Table. 5 summarizes the actionable design rules for each joint subcomponent, validated via theoretical analysis and parametric studies.

5.3. Validation metrics for joint design

In this study, the key joint performance evaluation indicators were as follows:

(i) Inter-story drift angle: ≤1/500 under design seismic loads, ensuring structural integrity;

(ii) Joint rotational stiffness: Discrepancy of less than 10% between the theoretical and FEA results;

(iii) Plastic deformation capacity: End-plate rotation of ≥ 0.02 rad without rupture, enabling energy dissipation.

These guidelines provide a structured framework for engineers to optimize joint design, balancing computational efficiency with mechanical accuracy in prefabricated steel structures.

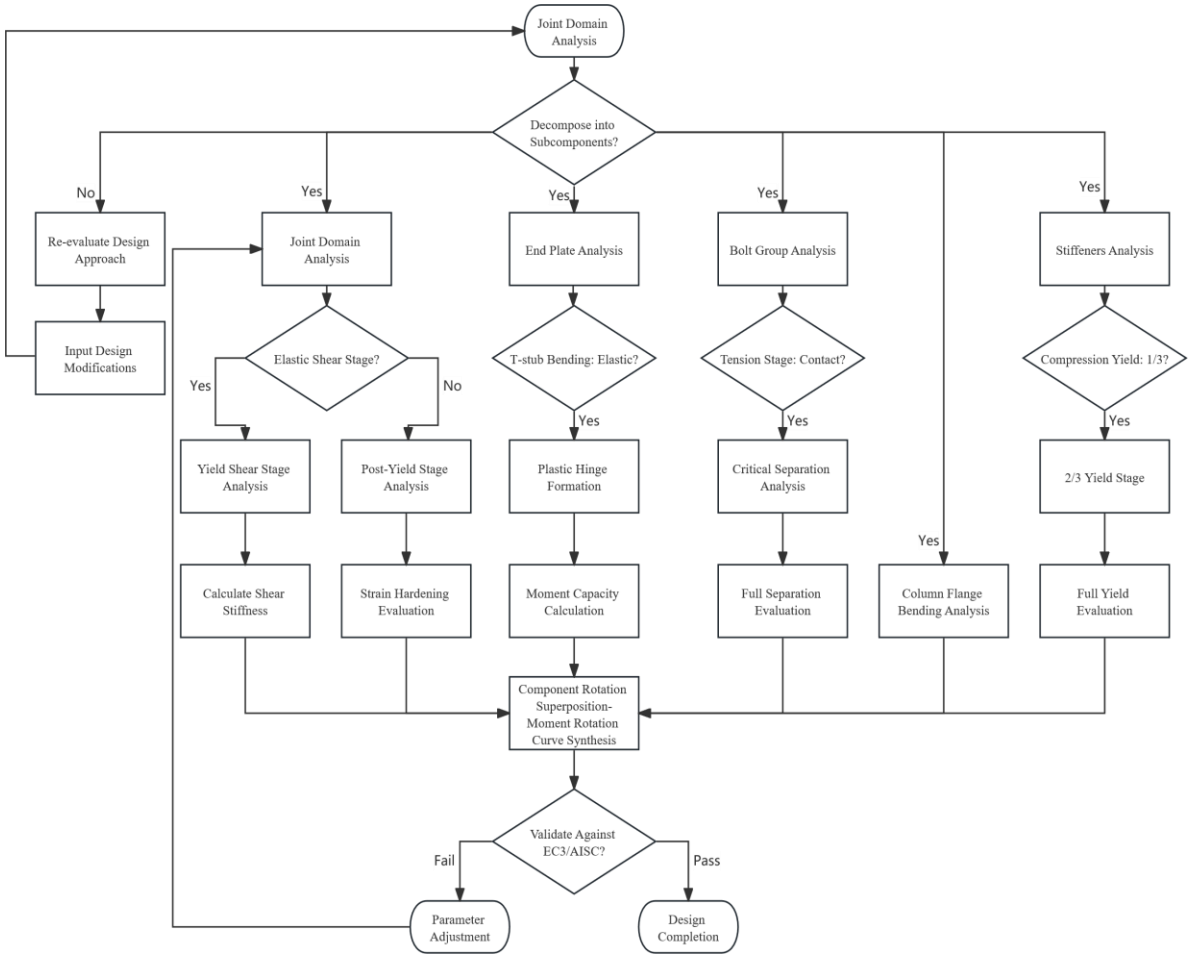

Fig. 33 Subcomponent-driven full-process design flow for beam-column joints

Table 5
Design rules and rationale for joint subcomponents

Subcomponent	Design Rule	Rationale
End plate	Use 12-16 mm for standard floors(plastic hinge development) ; 20-24 mm for seismic/critical floors (stiffness control).	Matches "strong-column/weak-joint" via thickness-dependent ductility.
Bolt group	Adopt 10.9-grade M20 bolts (pretension = 155 kN); symmetric double-row layout (spacing ≤ 3×bolt diameter).	Reduces lever effects (tested: >3d spacing increases bolt tension by over 15%).
Joint domain	Column web thickness ≥ 80% of end plate thickness.	Delays shear yielding to preserve initial stiffness (≥9×10³ kN·m/rad for seismic).
Column flange	Thickness matches end plate + 2 mm (e.g., 22 mm for 20 mm end plate).	Prevents flange failure before end plate/plastic hinges.
Stiffeners	Thickness ≥ 50% of end plate; mandatory in seismic zones.	Boosts compressive capacity (25% drop without stiffeners, per tests).

6. Conclusion

In this study, a theoretical analysis of the stress characteristics of an extended end plate bolted connection in steel frame beam-column joints was conducted. The theoretical calculation results were compared with FEM simulation results and existing studies. Based on the results, the main conclusions of this study can be summarized as follows:

1. The proposed full-process subcomponent analysis method effectively calculates the bearing capacity and deformation of individual components (joint domain, bolts, end plates, stiffeners) and synthesizes them to derive the joint's moment-rotation curve. This approach reduces reliance on complex FEM simulations, relying solely on component dimensions and material properties, making it suitable for engineering design - e.g., the Baoding Technician College steel frame project, where it guided the selection of end plate thickness (20 mm for ground floor; 16 mm for standard floors) and bolt configurations (symmetric double-row arrangements).

2. The thickness of end plates and column flanges significantly affects bolt internal forces: thinner plates (≤16 mm) amplify lever effects, leading to earlier end-plate plastic deformation, while thicker plates (≥20 mm) enhance the joint stiffness but require attention to the bolt tensile capacity. Three failure modes were identified: thin-plate yielding, medium-thick plate-bolt combined failure, and thick-plate bolt rupture.

3. Despite the fact that this study focused on the elastic and plastic stages, the proposed framework can be extended to include material-strengthening stages by incorporating strain-hardening parameters.

Acknowledgements

This work was financially supported by the Natural Science Foundation of Hebei Province (E2023208080).

References

[1] J Wang, L Han, et al. Hysteretic behaviour of flush end plate joints to concrete-filled steel tubular columns[J]. Journal of Constructional Steel Research, 2009, 65(8): 1644-1663.
[2] Yan S, Rasmussen K J R, Jiang L L, et al. Experimental evaluation of the full-range behaviour of steel beam-to-column connections[J]. Advanced Steel Construction, 2020, 16(1): 77-84.
[3] Shah S N R, Sulong N H R, Khan R, et al. Structural performance of boltless beam end connectors[J]. Advanced Steel Construction, 2017, 13(2): 144-159.
[4] ENV 1993-1-8:2005, Eurocode 3: Design of steel structures—Part 1.8: Design of joints.
[5] Y. O. Özkılıç. The capacities of unstiffened T-stubs with thin plates and large bolts. Journal of Constructional Steel research, 2021, 186:1-16.
[6] Y. O. Özkılıç, C. Topkaya. The plastic and the ultimate resistance of four-bolt extended end plate connections. Journal of Constructional Steel Research, 2021, 181: 106614.
[7] Zhang A L, Shangguan G H, Zhang Y X, et al. Experimental study of resilient prefabricated steel frame with all-bolted beam-to-column connections[J]. Advanced Steel Construction, 2020, 16(3): 255-271.
[8] JGJ/T 101-2015, Specification for test methods of seismic buildings, Architecture Industrial Press of China, Beijing, 2015.
[9] Gang Shi, Hao Fan, Yu Bai, et al. Improved measure of beam-to-column joint rotation in steel frames. Journal of Constructional Steel Research, 2012, 70: 298-307.
[10] Titoum M, Mazoz A, Benanane A, et al. Experimental study and finite element modelling of push-out tests on a new shear connector of I-shape[J]. Advanced Steel Construction, 2016, 12(4): 487-506.
[11] Lingli Pan, Yiyi Chen. Modified formula for calculating elastic stiffness of panel zone in H-shaped beam-column connections. Engineering Mechanics, 2016, 33(11): 68-74+94.
[12] GB 50017-2017, Steel Structure Design Standards. Architecture Industrial Press of China, Beijing, 2017.
[13] Ma H W, Zheng H, Zhang W, et al. Experimental and numerical study of mechanical properties for the double-ribbed reinforced beam-column connection[J]. Advanced Steel Construction, 2020, 16(4): 297-309.
[14] Sufang Wang, Yiyi Chen. Calculation of initial stiffness of beam-to-column end plate joint. Engineering Mechanics, 2008(08): 109-115.
[15] H. Krwinkler, V. M. Bertero, E. P. Popov. Shear Behavior of Steel Frame Joints. Journal of the Structural Division, 1975, 101(ST11).
[16] Torbaghan M K, Sohrabi M R, Kazemi H H. Investigating the behavior of specially pre-fabricated steel moment connection under cyclic loading[J]. Advanced Steel Construction, 2018, 14(3): 412-423.
[17] Bin Qin, Steel Structure Joint Design Manual. China Architecture & Building Press, Beijing, 2023.
[18] JGJ 82-2011, Technical specification for high strength bolt connection of steel structure, Architecture Industrial Press of China, Beijing, 2011.
[19] Macillo V, Shakeel S, Fiorino L, et al. Development and calibration of a hysteretic model for cfs strap braced stud walls[J]. Advanced Steel Construction, 2018, 14(3): 337-360.
[20] British Standards Institution, BS5950, Structural use of steelwork in building. British Constructional Steelwork Association, 2001.
[21] ANSI/ANSC 358-05, Prequalified Connections for Special and Intermediate Steel Moment Frames for Seismic Applications. American Institute of Steel Construction (AISC), Chicago, 2005.
[22] Patel V, Uy B, Pathirana S W, et al. Finite element analysis of demountable steel-concrete composite beams under static loading[J]. Advanced Steel Construction, 2018, 14(3): 392-411.
[23] GB51022-2015, Technical code for steel structure of light-weight building with gabled frames. Architecture Industrial Press of China, Beijing, 2015.
[24] Nouri K, Sulong N H R, Ibrahim Z, et al. Behaviour of novel stiffened angle shear connectors at ambient and elevated temperatures[J]. Advanced Steel Construction, 2021, 17(1): 28-38.
[25] Lele Sun, Xiaoxia Yang, Min Cai, et al. Monotonic bending behaviour of TOBs bolted beam to SHS column connection with stiffening component. Journal of Building Engineering 62 (2022) 105339.
[26] Lele Sun, Zeqi Liang, Qishuai Wang, et al. Seismic response on T-head square-neck one-side bolted endplate connection of beam to square tubular column. Engineering Structures 246 (2021) 113077.
[27] Baofeng Zheng, Dianhan Wu, Jiachang Wang, Ganping Shu. Test on seismic behaviors of stainless steel bolted extended end plate beam-column joints. Thin-Walled Structures 196 (2024) 111516.
[28] Li R, Jin J J, Xiao Z C, et al. Study on bending performance and load-carrying capacity of single-layer cylindrical reticulated shell with new sprayer joint[J]. Advanced Steel Construction, 2025, 21(1): 31-41.